JGR Solid Earth

RESEARCH ARTICLE
10.1029/2022JB024575

Magmatic and Tectonic Domains of Central Costa Rica and the Irazú-Turrialba Volcanic Complex Revealed by Ambient Noise Tomography

Elliot Amir Jiwani-Brown[1], Thomas Planès[1], Javier Francisco Pacheco[2], Mauricio M. Mora[3], and Matteo Lupi[1]

[1]Department of Earth Sciences, University of Geneva, Geneva, Switzerland, [2]Observatorio Vulcanológico y Sismológico de Costa Rica (OVSICORI), Universidad Nacional Costa Rica, Heredia, Costa Rica, [3]Red Sismológica Nacional (RSN), Escuela Centroamericana de Geología, Universidad de Costa Rica, San José, Costa Rica

Key Points:

- We compute a regional scale ambient noise tomography (ANT) for the Central Costa Rica Volcanic Front and a local scale ANT of the Irazú Turrialba Volcanic Complex (ITVC)
- We present an improved resolution of the subsurface structures including the shallow and intermediate depth magmatic reservoirs beneath the ITVC, interlinking conduits and internal plumbing systems of these volcanoes
- We show that for depths of up to 12 km, ANT can image large-scale subsurface features (>3 km) including magmatic bodies, mountain range roots, regions of deformation

Supporting Information:

Supporting Information may be found in the online version of this article.

Correspondence to:

E. A. Jiwani-Brown,
Elliot.Jiwani-Brown@unige.ch

Citation:

Jiwani-Brown, E. A., Planès, T., Pacheco, J. F., Mora, M. M., & Lupi, M. (2022). Magmatic and tectonic domains of Central Costa Rica and the Irazú-Turrialba volcanic complex revealed by ambient noise tomography. *Journal of Geophysical Research: Solid Earth*, *127*, e2022JB024575. https://doi.org/10.1029/2022JB024575

Received 12 APR 2022
Accepted 14 NOV 2022

Author Contributions:

Conceptualization: Elliot Amir Jiwani-Brown, Matteo Lupi
Data curation: Elliot Amir Jiwani-Brown, Thomas Planès, Javier Francisco Pacheco, Mauricio M. Mora, Matteo Lupi
Formal analysis: Elliot Amir Jiwani-Brown
Funding acquisition: Matteo Lupi
Investigation: Elliot Amir Jiwani-Brown
Methodology: Elliot Amir Jiwani-Brown, Thomas Planès, Matteo Lupi
Project Administration: Matteo Lupi

Abstract The Central America Volcanic Arc runs from Guatemala to Panama, locally interrupted in Costa Rica after the twin-system Irazú-Turrialba Volcanic Complex, at the onset of the Talamanca Cordillera. A marked geological discontinuity characterizes the transition between the volcanic arc and this continental mountain range. To shed light on the spatial and structural relationships between active tectonics and volcanism, we deployed a temporary network consisting of 20 broadband seismic stations around the Irazú-Turrialba Volcanic Complex that integrated the national seismic networks maintained by Costa Rican institutes. From the seismic records, we extract cross-correlation functions and Rayleigh wave group-velocity dispersion curves to perform two ambient noise tomographies at a regional and local scale. From this, we derive two models that point out the magmatic and tectonic features of the southern part of the Central American Volcanic Arc and of the Irazú-Turrialba Volcanic Complex. The regional-scale tomographic inversion suggests that such a volcanic complex shares a common reservoir at about 5–7 km depth that is fed by a sub-vertical region, departing from at least 12 km depth. From here magmas appear to be transported upwards and stored in separate reservoirs below each volcanic edifice. Our study establishes an improved understanding of the spatial relationship between tectonic features and distribution of magmatic reservoirs underpinning the plumbing system of the Irazú-Turrialba volcanic complex.

Plain Language Summary The line of volcanoes running from Guatemala to Panama are interrupted briefly in Costa Rica at the two volcanoes, Irazú and Turrialba. Here is a transition point between the volcanoes and the Talamanca mountain range. We installed a series of instruments that measure ground motion, around Irazú and Turrialba volcanoes. We supplemented this with other stations belonging to Costa Rican monitoring institutes. From the data, we observe how energy travels through the ground in the form of ambient noise, produced by natural and anthropogenic sources. This noise changes when traveling through subsurface features such as magma or fractures in the rock. We create images of the subsurface of Central Costa Rica and the Irazú and Turrialba volcanoes. We find large volumes of semi-liquid rock, possibly magma, surrounded by solid rock, beneath the volcanoes. Using the installed instruments, we improve the image resolution of the Irazú and Turrialba volcanoes beneath the ground. We also find features that correspond with large-scale ground/crustal deformation.

1. Introduction

Subduction driven processes in Costa Rica led to the development of volcanism, forming the active Central Costa Rican Volcanic Front (CCRVF). Located at the southernmost tip of the CCRVF is the active twin volcanic system, the Irazú-Turrialba Volcanic Complex (ITVC), 50 km north-east from Costa Rica's capital city, San Jose (Figure 1). The summits of each volcano are 10 km apart and form a complex that is about 60 km by 45 km at the base. To better understand these magmatic and tectonic domains, establishing the crustal structures beneath volcanic systems provides vital information into the implications of volcanism in Costa Rica.

Despite being geographically close, the Irazú and Turrialba volcanoes undergo different eruptive cycles. This may partially be explained by the complex magmatic interactions between different reservoirs at depth as highlighted by geochemical and petrological data (Alvarado et al., 2006; DeVitre et al., 2019). Alvarado et al. (2006) suggest that Irazú is fed by two distinct magmatic reservoirs evolving in parallel and occasionally mixing. The

Resources: Elliot Amir Jiwani-Brown, Javier Francisco Pacheco, Mauricio M. Mora
Software: Elliot Amir Jiwani-Brown, Thomas Planès
Supervision: Thomas Planès, Matteo Lupi
Validation: Elliot Amir Jiwani-Brown, Matteo Lupi
Visualization: Elliot Amir Jiwani-Brown, Matteo Lupi
Writing – original draft: Elliot Amir Jiwani-Brown
Writing – review & editing: Elliot Amir Jiwani-Brown, Thomas Planès, Javier Francisco Pacheco, Mauricio M. Mora, Matteo Lupi

main reservoir from which the mineral phases crystalize is proposed to be at about 12–15 km depth (Alvarado et al., 2006). This is supported by petrological data, suggesting andesitic magma is stored in a plumbing system at ∼13 km depth (Di Piazza et al., 2019), although such reservoirs are often perturbed by injections of deeper basaltic magmas (Alvarado et al., 2006). The plumbing system of Turrialba appears to be of similar complexity. DeVitre et al. (2019) highlight that the system is fed by multiple magmatic sources, with mixing between the back-arc and arc magmas believed to take place in the lower crust. In the shallower crust, mixing occurs within local andesitic reservoirs, differentiating over time (Alvarado et al., 2006).

Due to the two volcanoes varying in their magmatic composition (Benjamin et al., 2007; de Moor et al., 2016; Di Piazza et al., 2015), a difference in their respective eruptive activities is also observed (Di Piazza et al., 2015). Over recent years after more than 140 yr of dormancy, Turrialba went into unrest in 2010. The activity consisted of increased degassing, variations in fumarolic gas chemistry and seismic swarms (Campion et al., 2012; de Moor et al., 2016; Martini et al., 2010; Vaselli et al., 2010). Since 2016, however, eruptions have consisted of persistent ash emissions and regular, yet small, explosions. Irazú has a suggested volcanic cycle of about 200–400 yr (Alvarado et al., 2006) and appears to have been in a period of quiescence for about 50 yr (Epiard et al., 2017). The earliest reported eruptive activity at Irazú was marked by strombolian explosions at the beginning of its volcanic cycle, followed by phreatomagmatic explosions (Alvarado et al., 2006). Geological investigations of Costa Rican volcanism are well established and useful in producing an interpretation of the subsurface. Producing a distinct visual representation of magmatic features such as reservoirs or conduits beneath the visible surface expressions of volcanoes can be achieved through geophysical methods. They provide important and novel findings pertaining to the inner-workings of these complex crustal systems.

Previous passive seismic experiments in Costa Rica include studies of the Central Costa Rican Pacific subduction margin (Arroyo et al., 2009; Dinc et al., 2010; Husen et al., 2003), and also of the crustal structure within Central Costa Rica (Dzierma et al., 2010; Villegas Alvarez et al., 2019; Z. Yao et al., 1999). Active seismic experiments investigated the crustal structure across the CCRVF (Hayes et al., 2013). Unfortunately, detailed local earthquake tomographies have been hindered by the lack of homogeneously distributed seismic events that principally occur along the subduction interface. This led to the use of ambient noise tomography (ANT) to study large-scale crustal features in the region (Harmon et al., 2013; Nuñez et al., 2020). Nuñez et al. (2020) presented a regional scale, shear-wave velocity model of the shallow crust beneath Costa Rica. The study indicated large variability of shear-wave speeds within the crust, attributing it to the presence of deformation, fluid release and hydration along the volcanic arc in regions of recent eruptivity. The advantage of ANT is that it removes the reliance on earthquake sources, and can be applied in almost any location with an established and well-spread broadband seismic network (Macquet et al., 2014; Nicolson et al., 2012). Recent investigations have shown that ANT has become a widely used method in imaging earth subsurface structures across regional (Gao & Shen, 2015; Green et al., 2020; Nuñez et al., 2020; Shapiro et al., 2005) and local scales (Lin et al., 2013; Mordret et al., 2013). More importantly efforts have been made to determine smaller-scale structures within complex, heterogeneous, volcanic environments (Benediktsdóttir et al., 2017; Brenguier et al., 2007; Jeddi et al., 2017; Koulakov et al., 2014; Stankiewicz et al., 2010), making its application for investigating the volcanic environments of CCRVF and ITVC rather suited. Recent studies have shown the efficacy of ANT in highlighting magmatic and intrusive bodies as well as crustal-scale structures such as sedimentary basins and geologic lineament (Fallahi et al., 2017; González-Vidal et al., 2018; Planès et al., 2020). Special caution must be taken when using ANT, with the requirements of prior knowledge including initial reference velocity models, needed to constrain physical parameters. Observations of crustal lineaments are highly sensitive to variations in parameters such as the Poisson's ratio, which remains typically constant throughout the processing. Given that volcanic areas are highly heterogeneous, such over-simplifications could influence the efficacy of interpreting features including faults, magmatic bodies, and other dispersive structures.

Further geophysical methods deployed to investigate the crustal structure of Costa Rica include regional-scale gravity studies, mapping Bouguer gravity anomalies (Ander et al., 1991; Case, 1990; Kellogg et al., 1995; Lücke et al., 2010; Mickus, 2003). Besides the prominent negative large-scale anomalies found in Guatemala, Honduras, and Nicaragua, gravimetric studies have shown that a confined, negative anomaly exists beneath the southernmost Costa Rican volcanoes (Ponce & Case, 1987; Thorpe et al., 1981). Such variations have been further investigated by Lücke et al. (2010) who proposed a 3D density model of the upper crust of Costa Rica. These existing data helped establish key characteristics of the active volcanism occurring in the CCRVF (Hayes et al., 2013), including targeted experiments at the ITVC (DeVitre et al., 2019; Di Piazza et al., 2015).

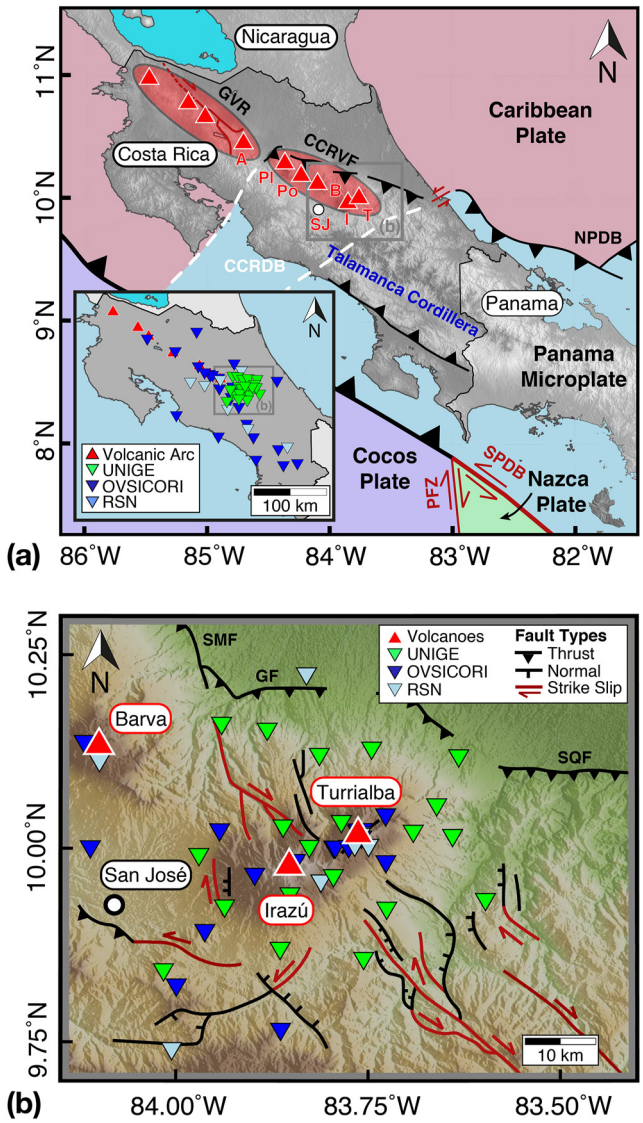

Figure 1. Tectonic Map of Costa Rica and surrounding regions. Key tectonic features adapted from Alvarado et al. (2017), Denyer (2009), and Montero et al. (2013) of (a) regional-scale, Central Costa Rica Volcanic Front, and (b) local-scale, Irazú-Turrialba Volcanic Complex. The key tectonic are shown: North Panama Deformation Boundary (NPDB), South Panama Deformation Boundary (SPDB), and Pacific Fracture Zone (PFZ). The large, white dashed line on the regional map represents the potential region of the Central Costa Rica Deformation Belt (CCRDB). The volcanic edifices (red triangles) include the Guanacaste Volcanic Range (GVR) and Central Costa Rica volcanic front (CCRVF). The marked volcanoes are Arenal (A), Platanar (Pl), Poás (Po), Barva (B), Irazú (I) and Turrialba (T). The seismic networks of OVSICORI, RSN, and UNIGE are shown by blue, azul, and green triangles.

The combination of previous geophysical, geochemical, and petrological methods have helped build an understanding of both the CCRVF and ITVC. Within this study, we aim to enhance on the work of previous studies, improving on interpretations of Costa Rica magmatic and tectonic domains, with particular focus given to the ITVC. We present a new, multi-scaled, shear wave velocity model, derived from ANT. We establish the model for the regional scale CCRVF, comparing to previous studies (Lücke et al., 2010; Nuñez et al., 2020) and an assessment to our methodology. With the deployment of a high-resolution network of broadband seismic stations, alongside the already established national network, we then present a novel, unprecedented image of the plumbing system of the ITVC, heightening the mapped resolution of its magmatic features. We improve the subsurface understanding of Irazú and Turrialba volcanoes, interpreting our findings in conjunction with previous multidisciplinary studies in the same region.

The manuscript is structured as follows. Section 2 provides a brief geological introduction of the investigated region. In Section 3, we describe the data processing workflow used in the retrieval of surface Rayleigh waves, the determination of surface wave dispersion curves and details of the method of inversion. Section 4 contains the results of the 2-step seismic inversion, comparing first the regional and local 2D group velocity maps, and then later the 3D shear-wave (Vs) model inversions for the local-scale tomography. The results are then discussed in Section 5.

2. Geological and Tectonic Setting and Previous Studies

The oblique subduction of the Cocos plate beneath the Caribbean plate led to the development of volcanism that formed the Central America Volcanic Arc (e.g., Álvarez-Gómez et al., 2019; Carvajal-Soto et al., 2020; DeMets, 2001; Kobayashi et al., 2014). To the northwest, the crust is topographically smoother, however to the southeast, a complex morphology of rougher crust exists as a succession of central seamounts and the Cocos ridge (Alvarado et al., 2007; Carr et al., 2003; Gazel et al., 2009; Hoernle et al., 2008). Several studies (Dzierma et al., 2011, 2010; Molnar & Sykes, 1969; Norabuena et al., 2004; Sallarès et al., 2000; Stoiber & Carr, 1973) shed light on the geological processes promoted by the convergence of the Cocos and Caribbean plates. GPS studies highlight complex ongoing deformation, uncovering the existence of the Panama micro-plate (Freymueller et al., 1993; Kellogg et al., 1995; Lundgren & Russo, 1996). The intimate link between tectonic processes, earthquakes, and volcano seismic activity has been shown to occur in Costa Rica (Arce, 2013; Bean et al., 2014; Lupi et al., 2014). A disputed deformation feature is that of the Central Costa Rica Deformation Belt (CCRDB; Carvajal-Soto et al., 2020). This deformation belt is defined as a complex, diffuse, active fault zone system, distinguishable by noticeable zones of strike-slip seismicity at shallow depths (<20 km) (Alvarado et al., 2017; Marshall et al., 2000; Montero, 2001; Montero et al., 2013), appearing to be the consequence of collision between the South American plate and island arc, formed by Costa Rica and Panama. This resulted in bending and eventual overriding of the Panama microplate, over the Caribbean plate (DeMets et al., 2010).

Volcanism in Costa Rica extends from the Nicaragua border (11.5°N) to western Panama (8°N). The CCRVF is formed by the Platanar-Porvenir complex, Poás, Barva, and the Irazú-Turrialba complex. Possible cooler wedge temperatures and broader, less concentrated regions of melt also contribute to volcanism observed along the volcanic front (Abers et al., 2014; Rychert et al., 2008; Syracuse et al., 2008). The indentation of the

subduction-resisting, buoyant, reheated Cocos ridge, younger oceanic Cocos plate, and its collision with the Panama microplate (LaFemina et al., 2009), results in a noticeable gap in volcanism (MacMillan et al., 2004; Protti et al., 1996), marking an important transition from a depleted oceanic arc to juvenile continental mass (Gazel et al., 2019). This coincides with the onset of the Talamanca Cordillera (Figure 1). Geochemical studies of the CCRVF reveal highly element enriched magmas associated with the subduction of offshore Galapagos traps (Gazel et al., 2009, 2021; Hoernle et al., 2008). However, volcanism as part of the volcanic arc continues into western Panama.

The geochemical and petrological diversity of volcanism within Costa Rica, and variation in eruptive output, suggests a spatially complex zone of magma storage, including zones of crystalline mush, mobile lenses of intrusive bodies for example, dykes and sills, and a higher crystal fraction framework (Ebmeier et al., 2018). Regions where magma storage zones are of an unknown structure and connectivity have been termed 'magmatic domains' (Ebmeier et al., 2018; Sigmundsson, 2016).

3. Data

We deployed 20 broadband seismic stations in a network surrounding the ITVC (Figure 1, Universtiy of Geneva—UNIGE). The sensors consisted of three-component Nanometrics Trillium Compact sensors (20 and 120 s). Our temporary network ran for a period of 11 months from deployment in April 2018 to removal in March 2019. All stations were equipped with Omnirecs DATA-CUBE3 digitizers, recording continuous ground motion at a sampling rate of 100 Hz. The study was supplemented by two regional permanent networks, namely 32 stations from the Observatorio Vulcanológico y Sismológico de Costa Rica (OVSICORI) of the Universidad Nacional Autonoma de Costa Rica and 12 from the Red Sismológica Nacional (RSN) of the Universidad de Costa Rica (RSN, 2011; Figure 1), giving us a total of 64 broadband seismic stations over this period.

3.1. Retrieving Rayleigh Waves

The data processing used in our study is performed with the routines developed by Planès et al. (2020) based on the workflow of Bensen et al. (2007). By cross-correlating ambient noise records from pairs of receivers, we estimate an empirical Green's function (Campillo & Paul, 2003; Lobkis & Weaver, 2001; Shen et al., 2012). Using vertical components of the continuous data, we section the records into 1h segments, apply a large-bandpass filter (20 s–4.5 Hz), and down sample the records to 10 Hz, accelerating subsequent computations. Next, we deconvolve the sensor response to calculate the instrument corrected ground-motion velocity at each sensor location, following the procedure of Haney et al. (2012). We reject any high-amplitude trace that can induce bias in the cross-correlation step of the ANT. These abnormal traces are normally attributed to earthquakes or strong localized activity. A "nominal" Root Mean Squared (RMS) method is computed by excluding the noisiest 10% of traces. Traces that show RMS amplitudes higher than 5 times the nominal RMS are removed. For some of the noisier stations, however, stricter ranges of acceptance were applied. The process of whitening, that is, normalization in the frequency domain, is applied to the selected data prior to cross-correlating station pairs and stacking over the full recording period (Bensen et al., 2007).

At this stage, to visualize the retrieved information, computed cross-correlation functions (CCFs) are stacked and sorted by inter-station distances (Figure 2a). By convention, the westernmost station of each pair was selected to be the virtual source. All traces are also band-pass filtered between 1 and 10 s and normalized by the maximum amplitude. The two most prominent tilted branches correspond to surface Rayleigh wave propagation. The branch at $t > 0$ s results from west-to-east propagating noise and at $t < 0$ s from east-to-west propagating noise. There is a visible asymmetry in the amplitude of these two branches suggesting that the prominent noise sources originate from the west, likely attributed to the Pacific Ocean. In comparison to previous studies (Liu et al., 2016; Planès et al., 2020), the asymmetry is not significant, with noise also generated by the Caribbean Sea. The central vertical branch is likely related to the arrival of teleseismic P waves ($t \sim 0$ s; Planès et al., 2020; Sheen & Shin, 2016; Singer et al., 2017; J. Zhang et al., 2010). This does not contaminate the surface wave noise responses except for shorter inter-station distances of approximately 1.5 λ. This is discussed later in the processing procedures.

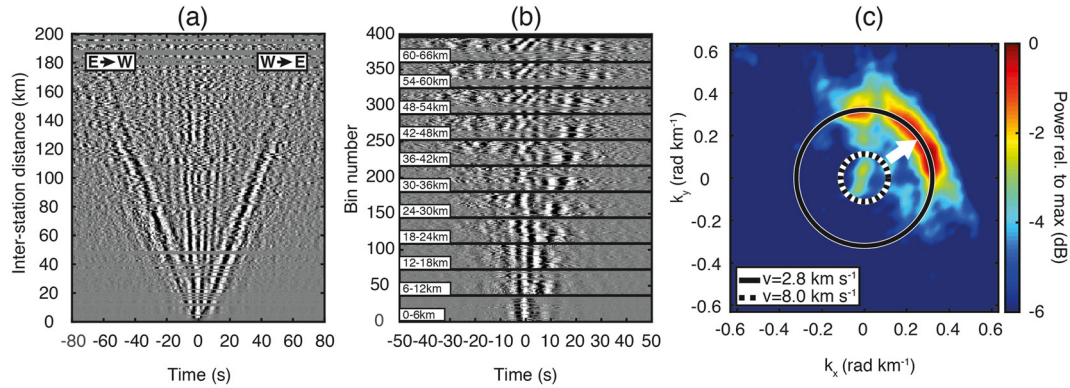

Figure 2. Signal directivity analysis. (a) Cross-correlation functions (CCFs) organized by inter-station distance. CCFs have been normalized and band pass filtered between 1 and 10 s. (b) Cross-correlation function plot organized by azimuths in bins of 6 km inter-station distances and 5° azimuth, (c) wave-vector decomposition allowing the study of noise directivity. The solid and dashed lines represent phase velocities 2.8 and 8.0 km s^{-1} respectively and correspond to the fundamental mode of the Rayleigh wave, computed at period $Tc = 7$ s. The white arrow shows the direction of propagation carrying the most energy (north-easterly), and the peak in the center possibly corresponds with noise-generated teleseismic *P* waves.

3.2. Noise Directivity Analysis

By organizing the CCFs based on their azimuthal dependence, an estimation of this directional bias can be realised (Figure 2b). Within each individual group of 12 km inter-station distances, there seems to be minor azimuthal bias depending on the prominence from Pacific or Caribbean. More details of this are provided in the Supporting Information (Figure S1 in Supporting Information S1). A wave vector decomposition approach is used to analyze the directivity of the coherent seismic noise. This is done by applying a 2D Fourier transform to the stacked CCFs. The decomposition is calculated at a period of 7 s, a frequency allowing for the avoidance of spatial aliasing with our network distribution. The dominant energy indicates propagation at a phase velocity of ~2.8 km s^{-1}, corresponding to the velocity of the Rayleigh wave fundamental mode estimated from a local 1D velocity model (Nazarian et al., 1983; Park et al., 1998; Rix, 1990; S. X. Zhang & Chan, 2003).

As shown in Figure 2c, the dominant direction of noise propagation is toward the north-east with an approximate bearing of 40°N, with further contributions ±45° of this direction. Although the CCFs reveal noise propagation from both the east and west, the wave vector decomposition shows dominant noise from the Pacific Ocean. Little energy is attributed to the Caribbean Sea. Cross-correlation and beam forming studies by Harmon et al. (2008) seem to support this observation, concluding that energy existing between 7 and 20 s are attributed to surface wave energy and in the shorter periods specifically, originate from the direction of the Pacific. The prominent period of energy is at $T = 7$s (Figure 2c). However, for other periods, we find the noise source more homogeneous. Noise from the wave vector decomposition support this (Figure S2 in Supporting Information S1), suggesting a prominent directionality encompassing an arc of azimuths between 0° and 90° for the dominant period, but also further contributions from the northwest (Figures S2e–S2g in Supporting Information S1) at greater azimuths. At $t > 10$ s, we see a significant decrease in energy, indicating a shift in noise from secondary to primary microseisms (Stehly et al., 2006; J. Zhang et al., 2010), leading to a reduction of Rayleigh wave energy (Nishida et al., 2008; Stankiewicz et al., 2010) and lose of directionality. This wave vector decomposition appears to correspond with the stacked CCFs (Figure 2a) and azimuthal dependant CCFs (Figure 2b), further strengthening the assumption that the seismic noise generated, mostly originates from the Pacific Ocean.

3.3. Group Velocity Dispersion Analysis

Frequency Time Analysis (Dziewonski et al., 1969, 1981; Keilis-Borok et al., 1989; Landisman et al., 1969) is used to extract group velocity dispersion curves, incorporating the Bensen et al. (2007) derived *instantaneous frequency correction* (Figure 3a). Further technical information are explained in the Supporting Information (Froment, 2011; Hansen, 1992; Tarantola, 2005; Tarantola & Valette, 1982). The surface wave traces are band-pass filtered through different bands up to 14 s (Figure 3b). We use the approach of (Mordret et al., 2014) to pick the fundamental mode. The surface wave traces are subject to a number of selection criteria; (a) inter-station

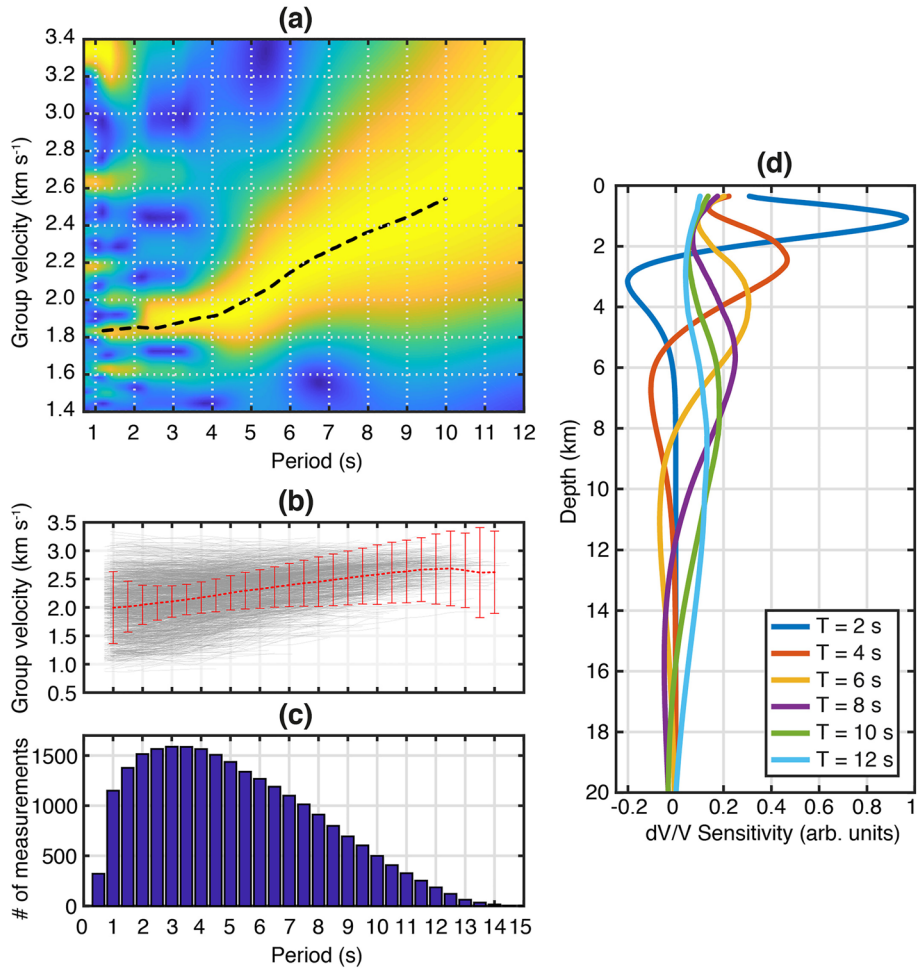

Figure 3. Dispersion curve. Example of group-velocity dispersion diagram. The dispersion diagram is obtained through Frequency Time Analysis (FTAN) decomposition of the cross-correlation function (CCF) between stations APW and VPEM. The dashed line shows the picked dispersion curve of the Rayleigh-wave fundamental mode between $T = 1$ s and $T = 10$ s. (b) All picked dispersion curves. The dashed red line represents the average picked dispersion curve with error bars representing the standard deviation of velocities at each period. (c) Number of measurement for each period. (d) Corresponding depth sensitivity kernels of the Rayleigh fundamental mode.

distance greater than 1.5 wavelengths, reducing the effects of wave distortion (Fallahi et al., 2017; Mordret et al., 2015; Obermann et al., 2016), (b) lower boundary of 1 s determined from preliminary pickings showing either cut or undecipherable data below 0.5 s and (c) categorization of the dispersion curves based on presence of overtones and continuity of fundamental mode & sensibilities of velocity ranges. These categories, and examples of dispersion curves fitting the criteria are detailed in the Supporting Information (see Section 1.2, Table S1, and Figure S3 in Supporting Information S1). When overtones are observed, the slowest mode is picked as the representation of the fundamental mode. Due to the lack of phase velocities, wavelength estimations are made using the picked group velocities. This might lead to an effective 1–1.5 wavelengths per inter-station distance (Lehujeur et al., 2016; Luo et al., 2015; Planès et al., 2020; Zigone et al., 2015). From the complete set of picked dispersion curves and number of measurements per period, good data coverage is observed for periods between 1 and 12 s (Figure 3c). Corresponding kernels are presented in (Figure 3d), showing group-velocity depth sensitivity of the Rayleigh fundamental mode. The subsurface model used to compute the kernels corresponds with the average model retrieved from the depth inversion described in Section 3.5.

Raypath maps and density plots at different periods (Figure 4) provide a visualization of the data coverage achieved. The colors of each raypath represent group-velocity of each station pair. The corresponding raypath

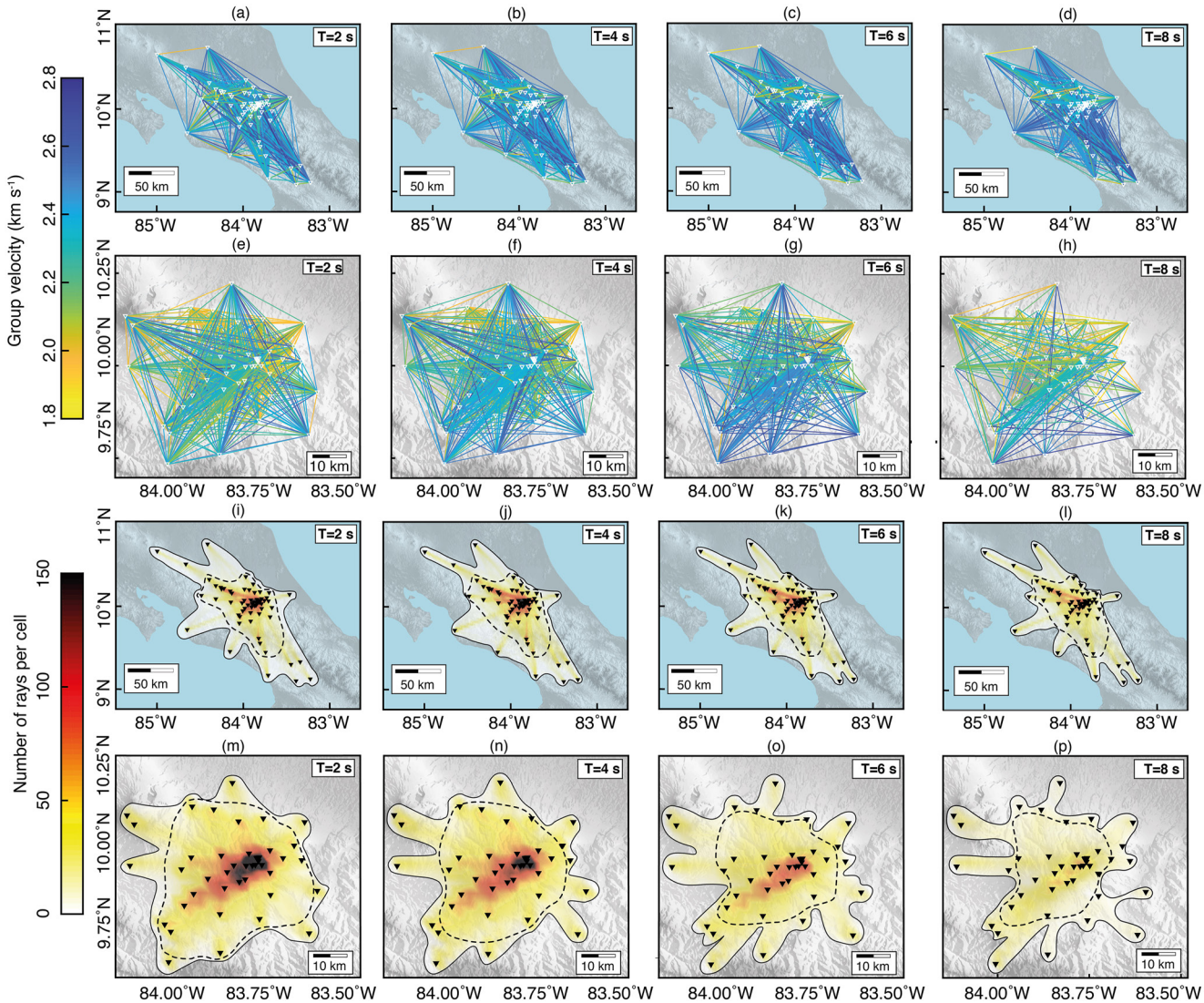

Figure 4. Raypath coverage. Raypath maps ((a–d) for regional, (e–h) for local) and corresponding raypath densities ((i–l) for regional, (m–p) for local) at periods 2, 4, 6, and 8 s. In the raypath density maps, the solid black-line contour delimits the areas where the number of rays per cell are greater than 5. The black dashed line is a manually established smoothed version of the black contour incorporating a level of qualitative interpretation.

densities (number of rays per cell) are used to define a lateral area of resolution for each network, and are used for the interpretation of the inversion data.

3.4. Inversion of 2D Group Velocity Maps

The spatial resolution tests are performed with checkerboard and spike tests (Figure 5, Figures S4 and S5 in Supporting Information S1) at both regional and local-scales, and are used with the raypath and density plots (Figure 4) to delineate a final interpretable area. From these tests, it is determined that a spatial resolution of ≥12–15 km for the regional maps can be achieved (Figure S4 in Supporting Information S1). A variable spatial resolution of ≥3–4 km for the local maps is determined, increasing with period (Figure S4 in Supporting Information S1). The resolution is improved in the center of the network and it is higher around the ITVC where the dense temporary network was deployed. Smearing occurs within the resolution tests as a result of distribution in the network (NW-SE regionally and NE-SW locally). The final cell size was chosen based on the smallest cell that was successfully resolved within both of these tests and a trade off between spatial resolution and number of rays-per-cell.

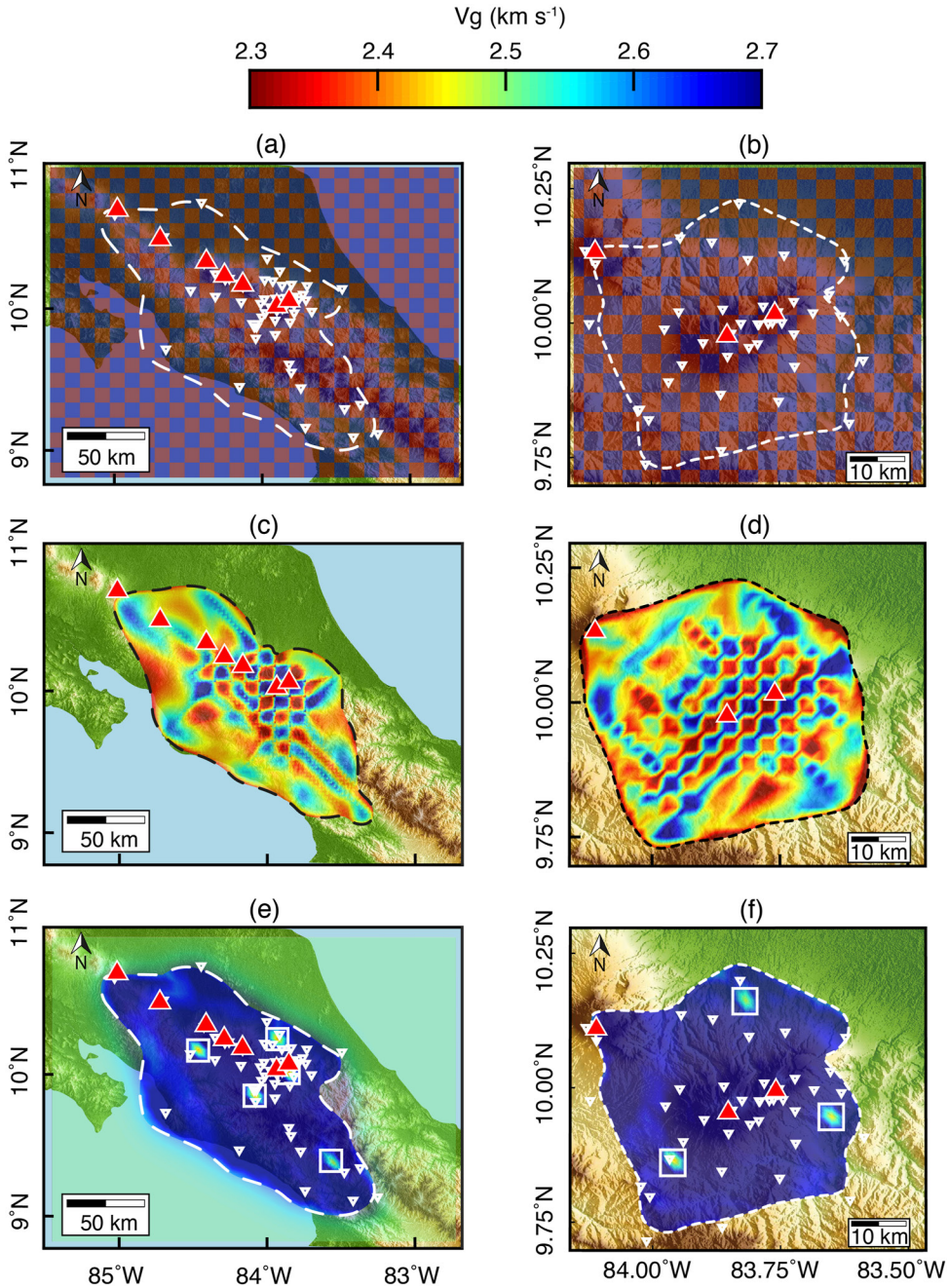

Figure 5. Resolution tests. (a) Regional and (b) local input of a checkerboard resolution test at $T = 4$ s consisting of alternating 12 km (regional model left column) and 3 km (local model right column) wide squares of low and high-velocity (2.3 and 2.7 km s^{-1} respectively). (c) Regional and (d) local output of checkerboard test. The pattern is successfully resolved within the previously defined area (dashed-line contour) except for the southwest boundary of the regional-scale map, coinciding with the northwest-southeast network alignment and lack of station coverage along the Caribbean coast. (e) Regional and (f) local spike resolutions test at $T = 8$ s. The synthetic input consists of a uniform velocity model (2.7 km s^{-1}) with 5 (regional) and 3 (local) single cells containing a low-velocity zone (2.3 km s^{-1}). These cells are indicated with solid white squares.

The first inversion step aims to retrieve group-velocity maps in the horizontal plane. For the regional network, a total of 66 inversions are performed at periods ranging from 1 to 14 s. For the local network, 46 inversions are computed between 1 and 10 s (both in steps of 0.2 s). We employ a regularized least squared inversion scheme, following Tarantola and Valette (1982). Throughout this initial inversion step, two important assumptions are

made. First, we consider straight-line ray propagation-paths between pairs of stations and second the influence of topography is assumed as negligible for travel-times.

After the first inversion step, a set of outliers (~5%–10% of the whole data set) were removed. These were defined as estimated data points that vary by more than 10% from the measured data points, based on RMS misfit. This provides further, more quantitative filtering of the picked dispersion curves established in Section 3.1. The first full inversion included all the picked dispersion curve data measurements, producing preliminary velocity maps that were subsequently used to estimate synthetic group-velocity data. This step allowed for the identification of a-posteriori outlying measurements corresponding to certain station pairs lying above the threshold of misfit. The second full inversion was done to produce the final 2D group velocity maps, removing outlier measurements, and thus removing anomalous station pairs dispersion curves.

3.5. Retrieval of 3D Shear-Wave Model Through Depth Inversion

To produce a realistic representation of seismic shear-wave velocity variations at depth, a further stage of inversion is needed. First, a set of effective group-velocity dispersion curves is constructed using the maps obtained after the first inversion stage. For each grid point, or node, in the 2D plane, these dispersion curves are assumed to be locally representative of the corresponding 1D shear-velocity depth profiles (Mordret et al., 2014; Obermann et al., 2013; Planès et al., 2020; Ritzwoller et al., 2011; Shapiro & Ritzwoller, 2002; Yang et al., 2008). The method established by Planès et al. (2020) relies on homogeneous, fixed-sized cells for the tomographic model.

To infer a local shear-wave velocity depth profile from its corresponding effective dispersion curve, a Monte-Carlo type inversion is used, based on and adapted from the "Neighborhood Algorithm" (Sambridge, 1999; Wathelet, 2005, 2008). The model space is defined by the number of layers being considered, with each layer having an assigned range of possible shear-wave velocities and depths, with the exception of the final layer that acts as a half-space (infinite depth). P wave velocities of the layers, V_p, are computed from a V_p/V_s ratio = 1.78. The density of the layer is calculated following Gardner's relation (Gardner et al., 1974). V_p and ρ have a much smaller influence on the Rayleigh-wave velocity than V_s, the fixed Poisson's ratio and density calculation model is an assumption that reduces the number of free parameters to 2 x $N_L - 1$ where N_L is the number of layers.

The number of model layers determines the size of the model space and is limited by computational time. For both the regional and local inversion, an initial model of $N_L = 6$ layers was chosen. Inversion tests were run with a greater number of layers but this proved to be an over-complication detrimental to the results, with the final model dominated by the initial model, rarely deviating from the initial layered structure. A further assumption to the 3D model was a minimum layer thicknesses of 200 m. The forward problem, that is, computing a theoretical dispersion curve from a candidate depth profile, is solved using the ***gpdc*** routine from the ***Geopsy*** package (Wathelet, 2008).

For each dispersion curve (cell in the 2D horizontal grid), the inversion process consists of (a) generation of large initial randomly distributed 1D velocity models, N_{ini}; (b) computation of synthetic dispersion curves of new models and evaluate the data misfit; (c) selection of best fitting models, N_b, randomly resampling in the neighborhood, N_r and (d) iteratively repeat from the second step, N_{iter} times or until the misfit drops below an assigned threshold. When resampling new models within a given cell, we use successive random walks (Sambridge, 1999) and at the end of the process, the inverted model is constructed as the average of the 100 best fitting models. One such 1D local inversion was run independently for every cell (x, y point) on the 2D map, the individual solutions being aggregated and smoothed to form the final 3D model (see Planès et al., 2020 for more details).

4. Results of the Tomographic Inversions: Group and Shear-Wave Velocity Maps

Group velocities calculated from the tomographic inversions for regional and local-scales are presented as horizontal slices showing lateral heterogeneities at periods of 2, 4, 6, and 8 s (Figure 6). Each period is related to a depth range, pertaining to the relationship between wavelengths and depth-penetration of surface waves. Therefore, longer periods suggest increasing depth of investigation. This can be seen from the sensitivity kernels (Figure 3d), shorter periods (e.g., 2 s) are most responsive to the upper km's of sediments, with deeper structures observable from longer periods. Generally also, the sensitivity to lateral heterogeneities decreases with increasing period (depth). Average group velocity ranges between 2.0 km s^{-1} at the lower (1 s) boundary and 2.8 km s^{-1}

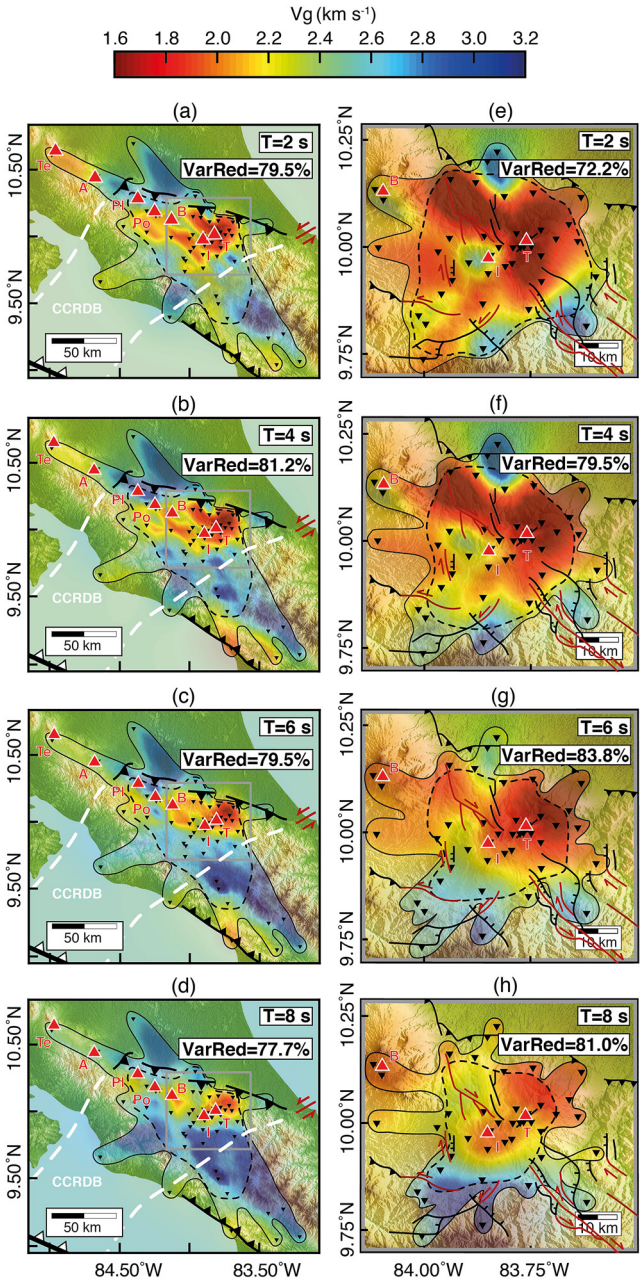

Figure 6. Regional and local 2D group velocity inversion. Inverted V_g maps for regional (a–d) and local-scale (e–f) at periods of $T = 2$ s, $T = 4$ s, $T = 6$ s, and $T = 8$ s. The solid (computerized interpretation) and dashed-line (qualitative interpretation) black contours encompass the area of good ray coverage that is expected to be well resolved. The variance-reduction of the final 2D inversion is also indicated as a percentage and is a statistical representation of variance between data generated within a homogeneous medium and mean picked group velocity, and observed model data. The seismic stations are shown by black triangles and the volcanic edifices (red triangles) are named from west to east as Tenorio, Arenal, Platanar, Poás, Barva, Irazú, and Turrialba, the last three of which appear on the local-scale maps.

at the upper (12 s) boundary period. However, particularly for the shorter periods with greater numbers of picked data (<6 s, Figure 3c), the range of individual picked velocities is wider at 1.5–3.0 km s^{-1}.

At the regional scale and at short periods (2–4 s, Figures 6a and 6b) we observe two distinct low-velocity regions, both sub-parallel to the direction of the volcanic arc. Moreover, to the north and to the south, the group velocities range between 2.6 and 3.2 km s^{-1}. At longer periods (6–8 s), the low-velocities appear as sub-circular regions beneath each active volcanic center (e.g., Barva, Irazú, and Turrialba). A contrast between the lower and higher group velocities, south of the ITVC, becomes prominent and particularly visible at 6 s. Similar low-velocities are observed on the local scale maps at all periods (2–8 s, Figures 6e–6h). At short periods (2–4 s, panels e–f in Figure 6) the low group velocities are prominent below the summit of Turrialba, with a noticeable high velocity below the Irazú summit. At longer periods (6–8 s, panels e–f in Figure 6) the low group velocities appear more rounded beneath both volcanoes, but prominent below that of Turrialba. Just at the limits of the local-scale resolution appears to be a transition from low to high velocity.

Following the procedure described in Section 3.5, we obtain a 3D, shear-wave velocity (V_S) model, extracting horizontal slices at 2 km depth intervals from 2 to 14 km. For the local inversion, we were unable to resolve at 14 km depth. The corresponding 2D V_S maps are shown for the regional scale in Figure 7, and for the local scale in Figure 8. We observe low V_S regions below the volcanic arc, consistent with Figures 6a–6d. This region appears beneath all volcanoes between Platanar to Irazú (between 4 and 7 km), elongated NW-SE (Figures 7b–7d). Below 8 km depth, this region is no longer visible beneath the ITVC and remains visible only below the currently active volcanic centers of Poás and Barva. The sharp contrast between high and low group velocities south of the ITVC shown in Figure 6d is also retrieved when inverting V_S velocities and occurs until about 8 km depth (Figure 7d). The inversion of ambient noise data retrieved from the high-resolution network deployed around the ITVC (Figure 8) benefits from a more refined grid spacing (Figure 5) than that of the regional results. At shallow depths (4–6 km) V_S velocities beneath the ITVC (Figures 8b and 8c) are about 2.6 km s^{-1}, in agreement with the values obtained for the same depth at the regional scale. This region narrows down below the ITVC at about 8–12 km depth (Figures 8d–8f). For depths >12 km, we found insufficient resolution in the data available to accurately represent shear wave velocities. We calculated a Root Mean Squared Error (RMSE) for solutions of our depth inversion to quantify the data fit and uncertainties in the V_s values (Figures 7 and 8g–8j), determining an average RMSE of ≈0.2–0.3 km s^{-1}.

Figure 9 shows the cross-sections along selected directions extracted from the inversion of the regional (Figures 9a–9c) and local (Figures 9d–9f) seismic data along with a comparison of our data against previous studies (Figures 9g and 9h). The cross sections include the ITVC (A-A' and D-D', Figures 9a and 9d), the upper crust perpendicular to the ITVC through Irazú volcano (B-B' and E-E', Figures 9b and 9e), and a transect of the CCRVF (C-C' and F-F', Figures 9c and 9f). We observe the lowest V_S regions ($V_S \leq 2.3$ km s^{-1}) at shallow depths (0–4 km), most prominently to the East of the ITVC. All the profiles of Figure 9 show that at 4 km depth a discontinuity occurs. This sudden sub-horizontal variation is particularly clear in Figures 9e and 9f and may be visible also in Figure 9c. The local-scale cross-sections (Figures 9d–9f) provide a refined picture of the region beneath Irazú and Turrialba volcanoes. Figure 9d shows three discernible regions of low-velocity with a

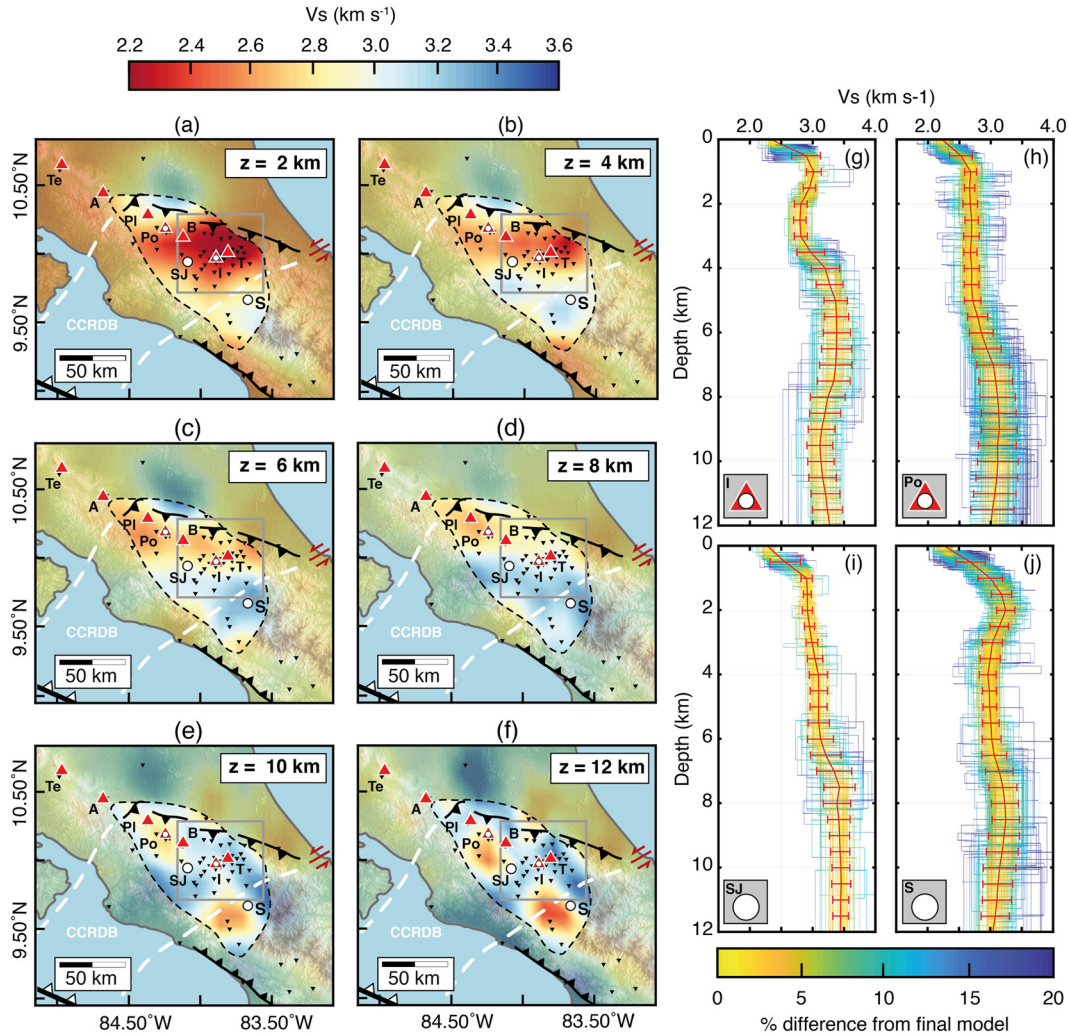

Figure 7. Inversion of the shear-wave velocity model at the regional scale. Horizontal slices of the 3D V_s model at depths of $z = 2$ km (a), $z = 4$ km (b), $z = 6$ km (c), $z = 8$ km (d), $z = 10$ km (e) and $z = 12$ km (f). The black dashed line frames the region where inversion is reliable. Some of the main tectonic features taken from Figure 1 and are also indicated. The seismic stations are shown by black triangles. The volcanic edifices (red triangles) are named from west to east as Tenorio (Te), Arenal (A), Platanar (Pl), Poás (Po), Barva (B), Irazú (I) and Turrialba (T). Results of the depth inversion at the locations of Irazú (g) and Poás (h) volcano, San Jose (i) and a location south of the volcanic arc (j). The red line represents the final V_s model with horizontal bars representing the Root Mean Squared Error with respect to the 2,000 best models calculated in the inversion. All models at each location are plotted indicating the % difference from the final model.

possible connection to low V_S velocity regions in the middle crust toward the west. With the exception of Platanar volcano, regions characterized by low V_S velocities are found until about 8 km depth (Figure 9c). The transition from the volcanic arc to the Talamanca Cordillera is marked by a sharp transition from low to high V_S velocity regions. This is particularly evident in Figure 9b.

5. Discussion

5.1. Underlying Assumptions of Ambient-Noise Tomography

Ambient-noise tomography requires a number of steps relying on physical assumptions, modeling approximations, and user-dependent choices that affect the outcome of the inversion. One physical assumption is that incoming noise has a sufficiently large directional coverage to provide enough reliable surface-wave travel times, a condition that we validated in Section 3.2. A stage of important user-influence is the dispersion curve picking, which provides the input data for the later inversions. This manual processing step requires the fundamental mode to

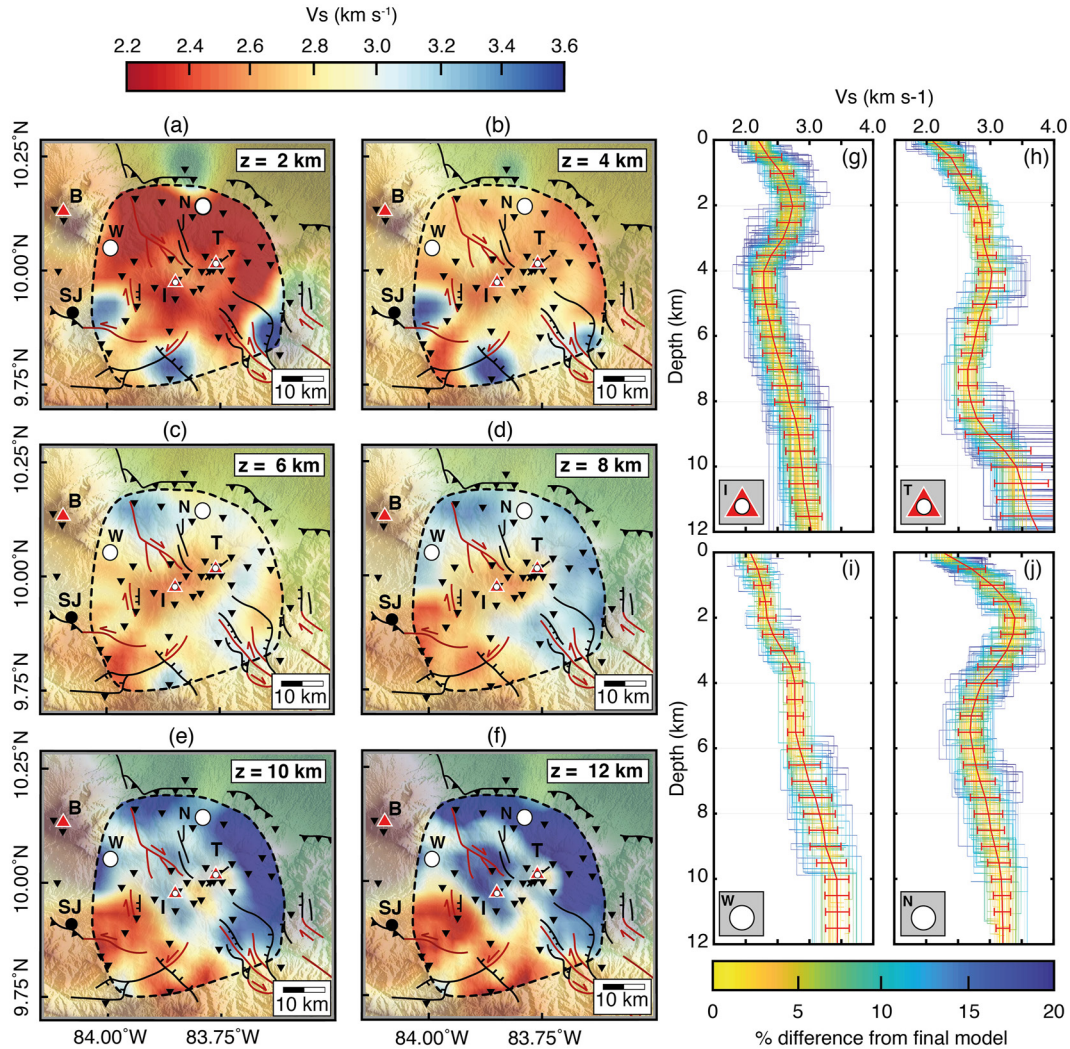

Figure 8. Inversion of the shear-wave velocity model at the local scale. 3D V_s model at depths of $z = 2$ km (a), $z = 4$ km (b), $z = 6$ km (c), $z = 8$ km (d), $z = 10$ km (e) and $z = 12$ km (f). The black dashed line is a further smoothed modified area of preferred resolution. The key tectonic features taken from Figure 1 and are also indicated. The seismic stations are shown by black triangles. The volcanic edifices (red triangles) are named from west to east as Barva (B), Irazú (I), and Turrialba (T). Results of the depth inversion at the locations of Irazú (g) and Turrialba (h) volcano, and a location west (i) and north (j) of the ITVC (j). The red line represents the final V_s model with horizontal bars representing the Root Mean Squared Error with respect to the 2,000 best models calculated in the inversion. All models at each location are plotted indicating the % difference from the final model.

be identified, an approach to removing station pairings affected by period or noise directionality biases. At short periods specifically, the distinction between fundamental mode and high-energy overtones sometimes proved difficult. We improved upon this by establishing a set of criteria (Section 3.3), aiding in the reproducibility of our results. The prominency of noise from the Pacific Ocean also produced similar issues, with stations perpendicular to this sometimes producing unreliable dispersion curves. In such instances where a fundamental mode could not be determined, we refrained from picking data, preferring no information to possible artifacts. It is important to clarify that many station pairs perpendicular to the defined prominent directionality of noise did provide surface wave dispersion curves stable enough for the later inversions, and the presence of a dominant source does not necessarily mean that noise may not exist elsewhere, as discussed for example by Yang et al. (2008) and H. Yao et al. (2008). Planès et al. (2020) noted that directional biases affect features elongated/striking along the incoming direction of the noise. Vice-versa, structures striking sub-perpendicularly (or at any given angle greater than 30°) to the direction of the incoming noise can be sampled. By comparing Figure 3 against the main strike of the volcanic arc shown in Figure 1, it is possible to assume that the main features investigated by the current

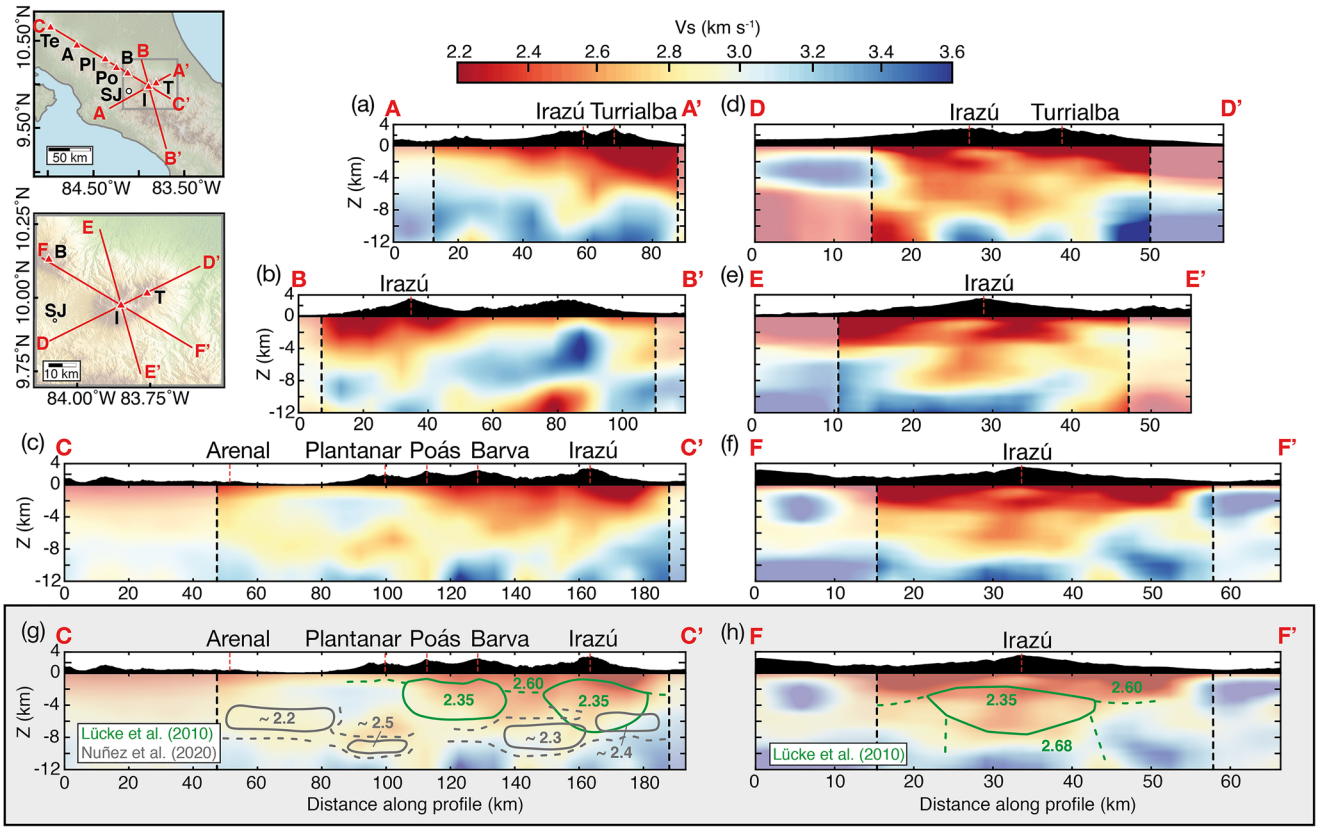

Figure 9. Cross-sections of the regional and local-scale velocity models. Regional (a–c) and local (d–f) cross sections of the 3D V_s model and comparison of C-C' (g) and F-F' (h) profiles with scaled results from the Nuñez et al. (2020) ambient noise tomography (ANT) study and Lücke et al. (2010) gravity density model. The black dashed lines delimit the area with good ray coverage and preferred inversion resolution. Red dashed lines mark the volcanic summits across which the cross-sections pass through.

manuscript are not sub-parallel to the propagation direction of the noise. For the longer periods of our records, we notice less energy (Figure 3c). We, therefore, expect that results for the wavevector decomposition with periods >10 s will lack resolution (Figures S2f–S2h in Supporting Information S1). However, despite stressing on the possible bias of our results at great depths, we decided to still include them in our inversion. Indeed, H. Yao et al. (2008) and Van Der Hilst (2009) concluded that for long time windows (months to years), noise directionality has little effect on the results.

As discussed in Harmon et al. (2010), inhomogeneous noise sources can cause a bias in the estimated velocities, with stations aligned to the prominent noise source producing faster values with respect to the true velocity. This however should be mitigated in part by the even spreading of our network, where the perpendicularly aligned stations evening out this bias. Harmon et al. (2008) also states that measurement errors due to heterogeneous sources and subsurface structures at shorter periods are smaller. We assessed and moderated for these errors through reduction of variance from the group velocity tomographic inversion, ensuring the bias in source directionality was removed, while preserving a high agreement between data and model.

We make two definitions of resolution; (a) determinable anomaly size and (b) lateral region of resolvable data. These are determined by the checkerboard (and spike) tests, and raypath densities (Figures 5 and 4). Grid sizes of 9 and 3 km (for regional and local scale respectively), which also act as the limits to the lateral anomaly sizes we can resolve from the 2D inversion process (Figure 5, Figures S4 and S5 in Supporting Information S1). This implies that potentially small and shallow reservoirs (≤2 km) cannot be explicitly interpreted with our data. The station distributions determine also our well-resolved lateral area for the inversion (Figure 4).

At the 2D inversion stage, we made two additional approximations. We did not account for surface topography, and surface-wave paths were modeled as straight rays. The true modeling of surface-wave travel-times in

3D media of arbitrary topography is a non-linear problem, computationally intensive and beyond the scope of this study. These approximations could imply that the shallow, small-wavelength anomalies could possibly be misplaced or have biased velocities, similarly to all ANT studies. The gathering of individual inversions of 1D velocity models from local dispersion curves before building the final 3D model is standard practice of ANT, with full 3D inversions computationally infeasible. This procedure may conflict with the strong lateral heterogeneities of volcanic environments. Dispersion curve inversion is also a non-unique problem where the operator is required to impose constraints on the possible output velocity models. For example, fixing the V_p/V_s ratio at 1.78 could present an over simplification for environments with significant lateral and vertical variations, such as the CCRVF and ITVC.

5.2. Tectonic Discontinuities

Prominent tectonic features in Costa Rica can appear in the ambient noise inversion as notable velocity contrasts. Mapped major tectonic features are displayed in Figures 7 and 8. The CCRDB, is a large-scale region of deformation driven by the northeast converging Panama Microplate (Alvarado et al., 2017; Kellogg et al., 1995; Trenkamp et al., 2002; Vargas & Mann, 2013). The CCRDB has no explicit boundaries, however implied limits are mapped in Figures 1, 6, and 7 based on various studies (Alvarado et al., 2017; Carvajal-Soto et al., 2020; Marshall et al., 2000; Montero et al., 2013). The implied northern limit of the CCRDB appears as a continuation of the North Panama Deformation Belt, represented by a series of fold-and-thrust faults (Figures 1, 6, and 7). Our observations, for both group (Figures 6a–6d) and shear (Figure 7) velocities, show that running sub-parallel to this northern boundary are shallow to intermediate low-velocity zones. Geodetic observations from inter-seismic crustal deformation suggests a similar northern limit (Carvajal-Soto et al., 2020; Marshall et al., 2000), although there is no geological evidence for this. These previous geodetic studies propose the southern limit to the CCRDB be at the transition between volcanic and continental mountain environment between the ITVC and Talamanca Cordillera. This is supported by recent neotectonic studies of the 1991 Mw 7.7 Limón earthquake (Montero-Pohly, 2021a) and the 1983 Cuericí and Buenavista earthquakes (Montero-Pohly, 2021b). The transition from ITVC to Talamanca Cordillera, is brought about by uplifted juvenile continental mass (Gazel et al., 2009, 2021, 2019), producing a break in the CCRVF, and a volcanic gap stretching into northern Panama (Carr et al., 2007; Sak et al., 2009). Our inversion is unable to confidently infer this southern limit, however, the noticeable contrast we observe in the southeast, from low to high V_S, up to a depth of 8 km (Figure 7) could present evidence of this transition between volcanic and mountain environments. This is supported by receiver function studies (Dzierma et al., 2010), finding discontinuous Moho morphologies at the CCRVF and Talamanca boundary. Proposed limits of the CCRDB from previous authors (Brandes et al., 2016; Vannucchi & Morgan, 2019) also correspond with our observations, although they did not identify such a sharp transition across the Talamanca Cordillera.

5.3. Velocity Structure of Central Costa Rica

We present a 3D shear-wave velocity model for the shallow and intermediate crustal structure of the CCRVF and ITVC at a regional scale, up to a depth of 12 km. Our main findings indicate a number of low-velocity zones linearly aligned with the axis of the volcanic front, and beneath the most recently active volcanoes in Central Costa Rica. Prominent, low shear-wave velocities appear in the upper 2 km of our inversion, on the flanks of the volcanic edifices in our study. We speculate that this may be caused by sedimentary basin and volcanic deposits (Folguera et al., 2016; González-Vidal et al., 2018; Kay & Ramos et al., 2006; Melnick & Echtler, 2006). These pronounced low V_S regions (bounded in Figure 10a by white dashed lines) seem to transition from a sedimentary into magmatic domain. Around the volcanic edifices, we also suggest that the low V_S velocity values may be related to the occurrence of hydrothermal systems fed by percolating groundwaters and fueled by particularly elevated geothermal gradients caused by magmas at depth.

Figure 10a presents a conceptual model for the CCRVF, proposing a more detailed interpretation of the magmatic domain of Costa Rica, with four major low-velocity zones (LV 1–4). LV1 occurs below Arenal volcano, seemingly interconnected with LV2 beneath Platanar and Poás volcanoes. LV3 and LV4 occur beneath Barva volcanoes and the ITVC, respectively. This model is supported by the gravity inversions of Lücke et al. (2010), and also in part by previous ambient-noise study in Costa Rica (Nuñez et al., 2020). Both are compared in Figure 9g, indicating the positions of low V_S zones and modeled crustal bodies against our results in profile C-C'. We find

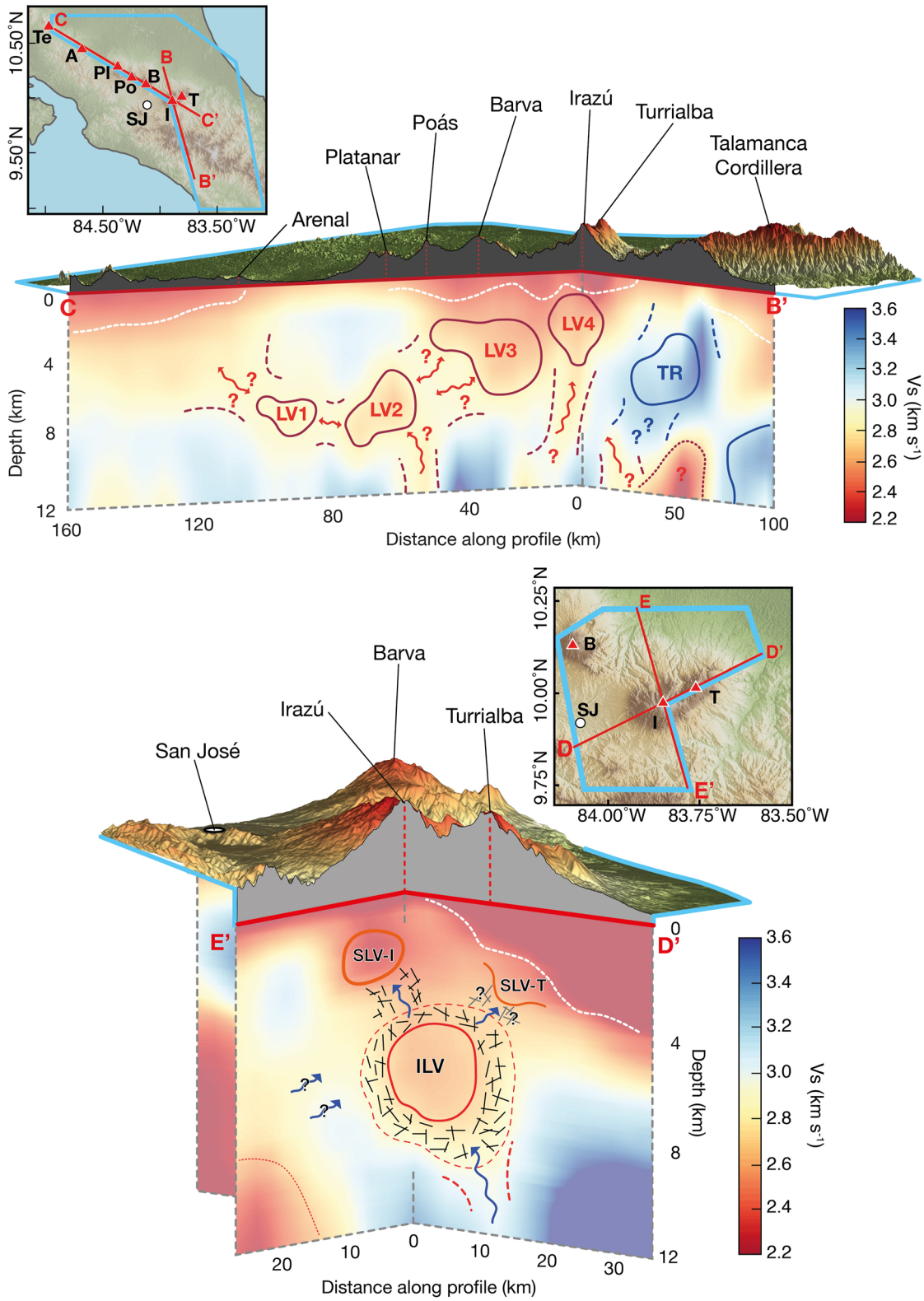

Figure 10. Regional and local conceptual models. Conceptual interpretations of the 3D V_s model for the regional-scale CCRVF (a) and local-scale ITVC (b). The limits of the low-velocity zones (LV 1–4), and magmatic transfer zones are marked by the dark-red dashed line and the Talamanca Range (TR) is marked by the blue dashed line. The limits of the intermediate low-velocity (ILV) zone beneath the ITVC and (smaller-) low-velocity (SLV) zones are marked by the red solid-circles, magmatic transfer zones also indicated. The LV and ILV limits are contours of $V_s = 2.7$ km s^{-1} and the red dotted line surrounding the ILV is a contour of $V_s = 2.9$ km s^{-1}. For both scales, the low-velocity zone attributed to sedimentary and magmatic deposits is marked by the white dashed line.

broad agreement between our inversion (LV3, Figure 10a) and the 2.35 kg m^{-3} modeled density anomaly of Lücke et al. (2010) below Poás and Barva, also coinciding with LV3 (Figure S6 in Supporting Information S1). Similarly, the region modeled by Lücke et al. (2010) below Irazú broadly corresponds to our observed V_S regions and LV4. The distribution of shear-wave velocities between our ambient noise inversion and that of Nuñez et al. (2020) are not in full agreement. This is particularly apparent beneath the ITVC, however this is likely due to our greater resolution from the improved network coverage. Nuñez et al. (2020) do have improved coverage to the northwest, closer to Nicaragua and Arenal volcano. It is important to note that Nuñez et al. (2020) incorporation of wavefront propagation theory does account for curved raypaths, contrasting to our assumed straight raypaths. Velocity ranges for high and low shear-wave velocities are comparable for both studies, and are similar to those retrieved from ambient-noise methods by previous authors in other volcanic areas, for example, in Chile (González-Vidal et al., 2018) and Indonesia (Fallahi et al., 2017).

We suggest that the deeper (≥3 km), low V_S velocity zones may indicate the presence of a ductile rheology probably caused by a mush zone hosting magmatic reservoirs, sub-volcanic conduits and enhanced permeability regions. We propose that this succession of low-velocity zones is related to a deformation region where deep magmas and slab-related fluids are focused into the upper crust. In this framework, low V_S velocity regions would be caused by fluid-rich, hot and almost ductile geological compartments hosting the deep plumbing systems of volcanoes as postulated by previous authors proposing regions of mush (Ebmeier et al., 2018; Edmonds et al., 2019) or thermally induced ductile domains (Cashman et al., 2017).

This succession of low-velocity zones, forming a deformation region, may be tectonically driven and prompted by the northeast convergence of the Panama microplate. This could promote the development of a young, pre-faulted upper crust that coincides with the strike of the CCRVF. Lücke et al. (2010) state that due to the high volumes and lateral extent of modeled bodies, the simple interpretation of magma chambers is unsustainable. This supports our proposal of intermediate-depth magmatism within a weakened, deformation zone. The occurrence of an incipient deformation zone hosting the volcanic arc is also supported by seismic data showing NW-SE strike-slip focal mechanisms at depths ≤20 km and above (Global CMT, Dziewonski et al., 1981; Ekström et al., 2012). This includes the M6.1 2009 Cinchona earthquake (Barrantes-Castillo et al., 2013).

5.4. Velocity Structure of the Irazú-Turrialba Volcanic Complex

We present a novel, local 3D shear-wave velocity model of the ITVC, defining the distribution of shear-wave velocities below the main volcanic edifice, up to 12 km depth (Figures 8 and 9d–9f). The lowest V_S values (2.2 km s^{-1}) appear to the northeast of Turrialba and suggest the presence of sedimentary units, an observation supported by Denyer and Alvarado (2007). Low V_S values south of Irazú could be related to the observed alignment of scoria, tuff and monogenetic cones in this region, following a similar N-S elongation Alvarado et al. (2006). This is supported by the numerical integration model of Carvajal-Soto et al. (2020), combining tectonic observations modified after Bird (2003), Marshall et al. (2000), and Kobayashi et al. (2014).

Figure 10b illustrates our proposed model for the ITVC, presenting a more detailed structure of the magma domain beneath both volcanoes. This domain consists of an intermediate low-velocity zone (ILV), connected to shallow low-velocity zones (SLV) below each volcanic edifice. The ILV is the most prominent feature determined by our tomographic inversion, and sits ∼12–10 km below the Irazú crater (6–8 km depth), seemingly fed by a deep-reaching conduit. The assumption that regions marked by low shear-wave velocities are purely magmatic bodies would imply the development of large caldera-like volcanic systems at the surface. This is not the case for the ITVC. Instead, we propose a complex system of shallow and intermediate magmatic reservoirs, surrounded by a region of a ductile domain and crystal mush, characteristic of the architectures and dynamics of trans-crustal magmatic systems (Cashman et al., 2017; Edmonds et al., 2019).

The limits to our proposed low-velocity zones are set at 2.7 km s^{-1} (solid red line, Figure 10b) for the potential partial melt, and 2.9 km s^{-1} for the larger ductile domain of crystal mush region (dashed red line, Figure 10b). These values are taken from theoretical studies of magmatic bodies (Christensen, 1996; Takei, 2002) and seismic tomography studies in volcanic environments similar to that of Costa Rica (González-Vidal et al., 2018; Obermann et al., 2016; Pritchard & Gregg, 2016; Stankiewicz et al., 2010). From this, we calculate theoretical volumes of ∼400–900 km^3 for the magmatic reservoirs and ductile mush zone. This is supported by smaller-scale, intermediate crustal depth magmatic regions, for example, in Laguna del Maule in Chile, derived from seismic

tomography methods (Bai et al., 2020; Wespestad et al., 2019). Estimations of 4%–6% for melt fraction of the Irazú and Turrialba volcanoes are found for basaltic andesitic volcanoes (Carr et al., 2007; Sadofsky et al., 2008), giving us approximations of partial melt of 16–54 km^3 for the ILV below the ITVC.

Alvarado et al. (2006) and DeVitre et al. (2019) detail the complex mixing of magma batches that have occurred for the more recent eruptions at Turrialba and Irazú respectively, both noting a shared basaltic-andesitic magmatic composition. Petrological data from andesitic magma of the El Retiro eruption (Di Piazza et al., 2019) suggests that the temperature and pressure conditions corresponded with a plumbing system at ∼12 km beneath the crater. This is in agreement with the location of our proposed ILV beneath the ITVC. Melt inclusion studies estimate water contents from both volcanoes at ∼3% (Benjamin et al., 2007; Di Piazza et al., 2019), which could equate to a shared reservoir at depth. This is supported by GPS (Battaglia et al., 2019) and gravity (Lücke et al., 2010), both models indicating that a shared body beneath both Irazú and Turrialba as the cause. Figure 9h compares the gravimetric data (Lücke et al., 2010) against our local-scale tomography, confirming what appears to be a general agreement between the low V_S values (ILV, Figure 10b and Figure S6b in Supporting Information S1), and the regions characterized by densities of 2.6 kg m^{-3} (Lücke et al., 2010). The gravimetric data below the ITVC suggests the occurrence of a low-density (possibly magmatic) formation roofing at about 2 km depth. This is in broad agreement with the distribution of our low-velocity, ductile domain.

From here it is possible to postulate magmatic transfer zones between multiple low V_S domains (ILV to the SLV-I and SLV-T), contributing to the diverse eruptive products of both volcanoes within the ITVC. Figure 9f suggests the existence of a shallower low-velocity zone at ∼5.5 km below the crater of Irazú. Alvarado et al. (2006) explain that the compositional diversity at Irazú is attributed to different magma batches at shallower levels, and indicates the presence of a shallower system (≤2 km depth) similar to that of the SLV-I. *S* wave velocity zones at Irazú volcano (Villegas Alvarez et al., 2019) also indicate a slow velocity region between 6 and 15 km, possibly indicative of our proposed ILV. However, they also report high-velocity zones perceived as cooled or dense volcanic rocks, at depths similar to our SLV-I. Due to the lack of recent activity at Irazú, the SLV-I could represent a region of fracturation, and previous magmatic storage that has since "dried", promoting these slower velocities. The sensitivity kernels of Figure 3d provide a measure of confidence that the presence of this shallower low-velocity zone is accurately represented in our inversion.

It is less clear to discern a similar feature below Turrialba volcano. However, the pronounced low V_S region attributed to sedimentary units on the eastern side of the Turrialba is deflected immediately below the volcanic cone, showing a step-like morphology (enhanced in the conceptual model of Figure 10b by the white dashed line). This shallow deflection, or flexure, at 2 km depth may be caused by a small shallow magmatic reservoir. Geodetic data, measuring ground deformation of the ITVC (Battaglia et al., 2019) suggests a more complex plumbing system is required, for example, a superficial reservoir, to satisfy the significant residual velocities at Turrialba, supporting the existence of the SLV-T. Seismicity attributed to SO_2 degassing (Conde et al., 2014) contribute to the schematic magmatic system devised by DeVitre et al. (2019). This schematic postulates an intermediate basaltic-andesitic magma storage region beneath Turrialba and Irazú, mixing with shallow rhyolitic residual magma from previous eruptive events (de Moor et al., 2016; DeVitre et al., 2019; Rizzo et al., 2016), supporting our proposal of the ILV and SLV-T.

We also observe a deeper emerging low-velocity zone just within the limits of model, at ∼10–12 km depth (Figures 8d and 8e), which could be the mid-crustal, principal feeding reservoir proposed by Alvarado et al. (2006) and Di Piazza et al. (2019). Profiles D-D', E-E' and F-F' (Figures 9d–9f) support these observations highlighting a southwards dipping low-velocity zone that we propose as the potential plumbing system feeding the ITVC. Outside of the ILV, and deeper emerging low-velocity feature, we observe shear-wave velocities increasing with depth. To the southeast, the transition toward the Talamanca Cordillera is marked by a defined shear-wave velocity contrast (Figures 9d and 9f).

Both the regional- and the local-scale inversions shown in our study seem to support a model where adjacent volcanic edifices may share a common reservoir at depth embedded in a ductile domain of mush and melt. Indeed, an increasing number of studies have recently suggested that neighboring volcanoes may not be considered as isolated systems but rather a ramification of deeper common middle-to lower-crust reservoir (Power et al., 2020). Similar observations were drawn by González-Vidal et al. (2018) who show how Andean volcanoes may be fed from a large-scale reservoir seated in the middle-crust, offset from the main volcanic edifice. At the large scale,

we observe such common reservoirs at Plantanar, Poás, and Barva volcanoes. At the local-scale, the common reservoir below the ITVC may further support this hypothesis.

6. Conclusions

We present a 3D shear-wave velocity model at the regional-scale of the Central Costa Rica Volcanic Front (CCRVF) and at the local-scale of the Irazú-Turrialba Volcanic Complex. We collected data from a temporary network deployed around the Irazú-Turrialba Volcanic Complex, supplemented by stations from permanent networks deployed across Costa Rica. The combination of the regional and local networks allowed us to perform two separate ambient-noise tomographies.

ANT reveals the existence of 4 significant low-velocity zones in the middle-to upper crust beneath the Arenal, Platanar, Poás, Barva, Irazú, and Turrialba volcanoes, representing magmatic reservoirs hosted within ductile lithologies. The formation of this region is attributed to the combination of volcanism and plate-scale deformation processes. We present a newer, comparable model of the volcanoes along the CCRVF, proposing that they share zones of weakened mush in the middle to upper crust, that in turn may feed shallower reservoirs that cannot be resolved by our regional-scale tomography. We also confirm the existence of a noticeable high-velocity zone below the Talamanca Range of southeast Costa Rica.

We present a novel high-resolution ANT image of the Irazú ITVC plumbing system, showing a common magmatic reservoir at about 5 km depth feeding two possible shallower reservoirs. Our results represent an unprecedented model of the subsurface structure of the ITVC, not yet reported at this scale or with such resolution and importantly, is also supported by previous, multidisciplinary studies. Our study helps toward a better understanding of the CCRVF and sheds light on the complex spatial distribution of magma below the Irazú-Turrialba Volcanic Complex.

Data Availability Statement

Data from all stations (temporary and permanent) for the acquisition period of April 2018 to March 2019 can be found in Matlab format under the DOI: https://doi.org/10.5281/zenodo.4912497.

Acknowledgments
This work was supported by a grant from the Swiss National Science Foundation (GENERATE, Grant 166900, PI Matteo Lupi). Thomas Planès was also supported by the same Grant. Seismic instrumentation of the RSN and the OVSICORI is financed by the National Emergency Law N° 8488. The maintenance of the RSN seismic stations comes from the following projects funded by the Vicerrectoría de Investigación of the Universidad de Costa Rica: "Vigilancia Sísmica de Costa Rica" (113-B5-704) and "Geofísica y Geodinámica Interna del Arco Volcánico de Costa Rica" (113-B5-A00). Fieldwork from OVSICORI was supported by project 0208-16 "Vigilancia de los volcanes de Costa Rica por medio de la actividad sísmica." Javier Francisco Pacheco and Mauricio Mora would like to thank technical support provided by Christian Garita, Antonio Mata, Daniel Rojas and Hairo Villalobos (OVSICORI) and Luis Fernando Brenes and Jean Paul Calvo (RSN) respectively. The authors would like to thank Antoine Haddad, Veronica Antunes and Francisco Muñoz (UNIGE) for their technical support with the data and in the field.

References

Abers, G. A., Fischer, K., Hirth, G., Wiens, D., Plank, T., Holtzman, B. K., et al. (2014). Reconciling mantle attenuation-temperature relationships from seismology, petrology, and laboratory measurements. *Geochemistry, Geophysics, Geosystems*, *15*(9), 3521–3542. https://doi.org/10.1002/2014gc005444

Alvarado, G. E., Benito, B., Staller, A., Climent, A., Camacho, E., Rojas, W., et al. (2017). The new Central American seismic hazard zonation: Mutual consensus based on up to day seismotectonic framework. *Tectonophysics*, *721*, 462–476. https://doi.org/10.1016/j.tecto.2017.10.013

Alvarado, G. E., Carr, M., Turrin, B. D., Swisher, C. C., Schmincke, H., & Hudnut, K. W. (2006). Recent volcanic history of Irazú volcano, Costa Rica: Alternation and mixing of two magma batches, and pervasive mixing. *Special Papers-Geological Society of America*, *412*, 259.

Alvarado, G. E., Soto, G., Pullinger, C. R., Escobar, R., Bonis, S., Escobar, D., & Navarro, M. (2007). Volcanic activity, hazards, and monitoring. *Central America: Geology, Resources and Hazards*, *2*, 1155–1188.

Álvarez-Gómez, J. A., Vázquez, A. S., Martínez-Díaz, J. J., Canora, C., Alonso-Henar, J., Insua-Arévalo, J. M., & Béjar-Pizarro, M. (2019). Push-pull driving of the Central America Forearc in the context of the Cocos-Caribbean-North America triple junction. *Scientific Reports*, *9*(1), 1–13. https://doi.org/10.1038/s41598-019-47617-3

Ander, M. E., Aiken, C. L., & Maricio, F. (1991). Regional gravity investigation of Honduras, Central America. *Journal of Volcanology and Geothermal Research*, *45*(1–2), 11–27. https://doi.org/10.1016/0377-0273(91)90019-v

Arce, M. F. (2013). Seismotectonic and the hipothetical strike-slip tectonic boundary of Central Costa Rica. *Earthquake research and analysis—New advances in seismology* (pp. 77–105). Intech Publications.

Arroyo, I. G., Husen, S., Flueh, E. R., Gossler, J., Kissling, E., & Alvarado, G. E. (2009). Three-dimensional *P* wave velocity structure on the shallow part of the Central Costa Rican Pacific margin from local earthquake tomography using off-and onshore networks. *Geophysical Journal International*, *179*(2), 827–849. https://doi.org/10.1111/j.1365-246x.2009.04342.x

Bai, T., Thurber, C., Lanza, F., Singer, B. S., Bennington, N., Keranen, K., & Cardona, C. (2020). Teleseismic tomography of the Laguna del Maule volcanic field in Chile. *Journal of Geophysical Research: Solid Earth*, *125*(8), e2020JB019449. https://doi.org/10.1029/2020jb019449

Barrantes-Castillo, G., Jiménez-Campos, C., & Ocón-García, M. J. (2013). Deslizamientos provocados por el terremoto de Cinchona de 2009, Costa Rica. *Revista Geográfica de América Central*, *2*(51), 89–100.

Battaglia, M., Alpala, J., Alpala, R., Angarita, M., Arcos, D., Euillades, L., et al. (2019). Monitoring volcanic deformation. *Reference module in Earth systems and environmental sciences*. Elsevier B. https://doi.org/10.1016/b978-0-12-409548-9.10902-9

Bean, C. J., De Barros, L., Lokmer, I., Métaxian, J.-P., O'Brien, G., & Murphy, S. (2014). Long-period seismicity in the shallow volcanic edifice formed from slow-rupture earthquakes. *Nature Geoscience*, *7*(1), 71–75. https://doi.org/10.1038/ngeo2027

Benediktsdóttir, Á., Gudmundsson, Ó., Brandsdóttir, B., & Tryggvason, A. (2017). Ambient noise tomography of Eyjafjallajökull volcano, Iceland. *Journal of Volcanology and Geothermal Research*, *347*, 250–263. https://doi.org/10.1016/j.jvolgeores.2017.09.017

Benjamin, E. R., Plank, T., Wade, J. A., Kelley, K. A., Hauri, E. H., & Alvarado, G. E. (2007). High water contents in basaltic magmas from Irazú volcano, Costa Rica. *Journal of Volcanology and Geothermal Research*, *168*(1–4), 68–92. https://doi.org/10.1016/j.jvolgeores.2007.08.008

Bensen, G., Ritzwoller, M., Barmin, M., Levshin, A. L., Lin, F., Moschetti, M., et al. (2007). Processing seismic ambient noise data to obtain reliable broad-band surface wave dispersion measurements. *Geophysical Journal International*, *169*(3), 1239–1260. https://doi.org/10.1111/j.1365-246x.2007.03374.x

Bird, P. (2003). An updated digital model of plate boundaries. *Geochemistry, Geophysics, Geosystems*, *4*(3). https://doi.org/10.1029/2001gc000252

Brandes, C., Tanner, D. C., & Winsemann, J. (2016). Kinematic 3D retro-modeling of an orogenic bend in the South Limón fold-and-thrust belt, eastern Costa Rica: Prediction of the incremental internal strain distribution. *Pure and Applied Geophysics*, *173*(10), 3341–3356. https://doi.org/10.1007/978-3-319-51529-8_8

Brenguier, F., Shapiro, N. M., Campillo, M., Nercessian, A., & Ferrazzini, V. (2007). 3D surface wave tomography of the Piton de la Fournaise volcano using seismic noise correlations. *Geophysical Research Letters*, *34*(2). https://doi.org/10.1029/2006gl028586

Campillo, M., & Paul, A. (2003). Long-range correlations in the diffuse seismic coda. *Science*, *299*(5606), 547–549. https://doi.org/10.1126/science.1078551

Campion, R., Martinez-Cruz, M., Lecocq, T., Caudron, C., Pacheco, J., Pinardi, G., et al. (2012). Space-and ground-based measurements of sulfur dioxide emissions from Turrialba volcano (Costa Rica). *Bulletin of Volcanology*, *74*(7), 1757–1770. https://doi.org/10.1007/s00445-012-0631-z

Carr, M., Feigenson, M., Patino, L., & Walker, J. (2003). Volcanism and geochemistry in Central America: Progress and problems. *Geophysical Monograph-American Geophysical Union*, *138*, 153–174. https://doi.org/10.1029/138gm09

Carr, M., Patino, L. C., & Feigenson, M. D. (2007). Petrology and geochemistry of lavas. *Central America: Geology, Resources, and Hazards*, *1*, 565–577.

Carvajal-Soto, L. A., Ito, T., Protti, M., & Kimura, H. (2020). Earthquake potential in Costa Rica using three scenarios for the Central Costa Rica deformed belt as western boundary of the Panama microplate. *Journal of South American Earth Sciences*, *97*, 102375. https://doi.org/10.1016/j.jsames.2019.102375

Case, J. (1990). *Caribbean crustal provinces; seismic and gravity evidence*. The Caribbean Region.

Cashman, K. V., Sparks, R. S. J., & Blundy, J. D. (2017). Vertically extensive and unstable magmatic systems: A unified view of igneous processes. *Science*, *355*(6331). https://doi.org/10.1126/science.aag3055

Christensen, N. I. (1996). Poisson's ratio and crustal seismology. *Journal of Geophysical Research: Solid Earth*, *101*(B2), 3139–3156. https://doi.org/10.1029/95jb03446

Conde, V., Bredemeyer, S., Duarte, E., Pacheco, J. F., Miranda, S., Galle, B., & Hansteen, T. H. (2014). SO_2 degassing from Turrialba volcano linked to seismic signatures during the period 2008–2012. *International Journal of Earth Sciences*, *103*(7), 1983–1998. https://doi.org/10.1007/s00531-013-0958-5

DeMets, C. (2001). A new estimate for present-day Cocos-Caribbean plate motion: Implications for slip along the Central American Volcanic Arc. *Geophysical Research Letters*, *28*(21), 4043–4046. https://doi.org/10.1029/2001gl013518

DeMets, C., Gordon, R. G., & Argus, D. F. (2010). Geologically current plate motions. *Geophysical Journal International*, *181*(1), 1–80. https://doi.org/10.1111/j.1365-246x.2009.04491.x

de Moor, J. M., Aiuppa, A., Avard, G., Wehrmann, H., Dunbar, N., Muller, C., et al. (2016). Turmoil at Turrialba volcano (Costa Rica): Degassing and eruptive processes inferred from high-frequency gas monitoring. *Journal of Geophysical Research: Solid Earth*, *121*(8), 5761–5775. https://doi.org/10.1002/2016jb013150

Denyer, P. (2009). *Atlas tectónico de Costa Rica*. Editorial de la Universidad de Costa Rica. Retrieved from https://books.google.co.uk/books?id=nm6LzQEACAAJ

Denyer, P., & Alvarado, G. E. (2007). Mapa geológico de Costa Rica. Escala 1: 400,000.

DeVitre, C. L., Gazel, E., Allison, C. M., Soto, G., Madrigal, P., Alvarado, G. E., & Lücke, O. H. (2019). Multi-stage chaotic magma mixing at Turrialba volcano. *Journal of Volcanology and Geothermal Research*, *381*, 330–346. https://doi.org/10.1016/j.jvolgeores.2019.06.011

Dinc, A. N., Koulakov, I., Thorwart, M., Rabbel, W., Flueh, E. R., Arroyo, I., et al. (2010). Local earthquake tomography of Central Costa Rica: Transition from seamount to ridge subduction. *Geophysical Journal International*, *183*(1), 286–302. https://doi.org/10.1111/j.1365-246x.2010.04717.x

Di Piazza, A., Rizzo, A., Barberi, F., Carapezza, M., De Astis, G., Romano, C., & Sortino, F. (2015). Geochemistry of the mantle source and magma feeding system beneath Turrialba volcano, Costa Rica. *Lithos*, *232*, 319–335. https://doi.org/10.1016/j.lithos.2015.07.012

Di Piazza, A., Vona, A., Mollo, S., De Astis, G., Soto, G. J., & Romano, C. (2019). Unsteady magma discharge during the "El Retiro" subplinian eruption (Turrialba volcano, Costa Rica): Insights from textural and petrological analyses. *Journal of Volcanology and Geothermal Research*, *371*, 101–115. https://doi.org/10.1016/j.jvolgeores.2019.01.004

Dzierma, Y., Rabbel, W., Thorwart, M. M., Flueh, E. R., Mora, M., & Alvarado, G. E. (2011). The steeply subducting edge of the Cocos ridge: Evidence from receiver functions beneath the northern Talamanca Range, south-Central Costa Rica. *Geochemistry, Geophysics, Geosystems*, *12*(4). https://doi.org/10.1029/2010gc003477

Dzierma, Y., Thorwart, M. M., Rabbel, W., Flueh, E. R., Alvarado, G., & Mora, M. (2010). Imaging crustal structure in south-Central Costa Rica with receiver functions. *Geochemistry, Geophysics, Geosystems*, *11*(8). https://doi.org/10.1029/2009gc002936

Dziewonski, A., Bloch, S., & Landisman, M. (1969). A technique for the analysis of transient seismic signals. *Bulletin of the Seismological Society of America*, *59*(1), 427–444. https://doi.org/10.1785/bssa0590010427

Dziewonski, A., Chou, T.-A., & Woodhouse, J. H. (1981). Determination of earthquake source parameters from waveform data for studies of global and regional seismicity. *Journal of Geophysical Research: Solid Earth*, *86*(B4), 2825–2852. https://doi.org/10.1029/jb086ib04p02825

Ebmeier, S., Andrews, B., Araya, M., Arnold, D., Biggs, J., Cooper, C., et al. (2018). Synthesis of global satellite observations of magmatic and volcanic deformation: Implications for volcano monitoring and the lateral extent of magmatic domains. *Journal of Applied Volcanology*, *7*(1), 1–26. https://doi.org/10.1186/s13617-018-0071-3

Edmonds, M., Cashman, K. V., Holness, M., & Jackson, M. (2019). *Architecture and dynamics of magma reservoirs*. The Royal Society Publishing.

Ekström, G., Nettles, M., & Dziewoński, A. (2012). The global CMT project 2004–2010: Centroid-moment tensors for 13,017 earthquakes. *Physics of the Earth and Planetary Interiors*, *200*, 1–9. https://doi.org/10.1016/j.pepi.2012.04.002

Epiard, M., Avard, G., de Moor, J. M., Martinez Cruz, M., Barrantes Castillo, G., & Bakkar, H. (2017). Relationship between diffuse CO_2 degassing and volcanic activity. Case study of the Poás, Irazú, and Turrialba volcanoes, Costa Rica. *Frontiers of Earth Science*, *5*, 71. https://doi.org/10.3389/feart.2017.00071

Fallahi, M. J., Obermann, A., Lupi, M., Karyono, K., & Mazzini, A. (2017). The plumbing system feeding the Lusi eruption revealed by ambient noise tomography. *Journal of Geophysical Research: Solid Earth*, *122*(10), 8200–8213. https://doi.org/10.1002/2017jb014592

Folguera, A., Naipauer, M., Sagripanti, L., Ghiglione, M. C., Orts, D. L., & Giambiagi, L. (2016). *Growth of the Southern Andes*. Springer.

Freymueller, J. T., Kellogg, J. N., & Vega, V. (1993). Plate motions in the North Andean region. *Journal of Geophysical Research: Solid Earth*, *98*(B12), 21853–21863. https://doi.org/10.1029/93jb00520

Froment, B. (2011). Utilisation du bruit sismique ambiant dans le suivi temporel de structures géologiques (Doctoral dissertation, Université de Grenoble). Retrieved from https://tel.archives-ouvertes.fr/tel-00648796

Gao, H., & Shen, Y. (2015). A preliminary full-wave ambient-noise tomography model spanning from the Juan de Fuca and Gorda spreading centers to the Cascadia volcanic arc. *Seismological Research Letters*, *86*(5), 1253–1260. https://doi.org/10.1785/0220150103

Gardner, G., Gardner, L., & Gregory, A. (1974). Formation velocity and density—The diagnostic basics for stratigraphic traps. *Geophysics*, *39*(6), 770–780. https://doi.org/10.1190/1.1440465

Gazel, E., Carr, M., Hoernle, K., Feigenson, M. D., Szymanski, D., Hauff, F., & Van Den Bogaard, P. (2009). Galapagos-OIB signature in southern Central America: Mantle refertilization by arc-hot spot interaction. *Geochemistry, Geophysics, Geosystems*, *10*(2). https://doi.org/10.1029/2008gc002246

Gazel, E., Flores, K. E., & Carr, M. (2021). Architectural and tectonic control on the segmentation of the Central American Volcanic Arc. *Annual Review of Earth and Planetary Sciences*, *49*. https://doi.org/10.1146/annurev-earth-082420-055108

Gazel, E., Hayes, J. L., Ulloa, A., Alfaro, A., Coleman, D. S., & Carr, M. (2019). The record of the transition from an oceanic arc to a young continent in the Talamanca Cordillera. *Geochemistry, Geophysics, Geosystems*, *20*(6), 2733–2752. https://doi.org/10.1029/2018gc008128

González-Vidal, D., Obermann, A., Tassara, A., Bataille, K., & Lupi, M. (2018). Crustal model of the Southern Central Andes derived from ambient seismic noise Rayleigh-wave tomography. *Tectonophysics*, *744*, 215–226. https://doi.org/10.1016/j.tecto.2018.07.004

Green, R. G., Sens-Schönfelder, C., Shapiro, N., Koulakov, I., Tilmann, F., Dreiling, J., et al. (2020). Magmatic and sedimentary structure beneath the Klyuchevskoy volcanic group, Kamchatka, from ambient noise tomography. *Journal of Geophysical Research: Solid Earth*, *125*(3), e2019JB018900. https://doi.org/10.1029/2019jb018900

Haney, M. M., Power, J., West, M., & Michaels, P. (2012). Causal instrument corrections for short-period and broadband seismometers. *Seismological Research Letters*, *83*(5), 834–845. https://doi.org/10.1785/0220120031

Hansen, P. C. (1992). Analysis of discrete ill-posed problems by means of the L-curve. *SIAM Review*, *34*(4), 561–580. https://doi.org/10.1137/1034115

Harmon, N., Cruz, M. S. D. L., Rychert, C. A., Abers, G., & Fischer, K. (2013). Crustal and mantle shear velocity structure of Costa Rica and Nicaragua from ambient noise and teleseismic Rayleigh wave tomography. *Geophysical Journal International*, *195*(2), 1300–1313. https://doi.org/10.1093/gji/ggt309

Harmon, N., Gerstoft, P., Rychert, C. A., Abers, G. A., Salas de La Cruz, M., & Fischer, K. M. (2008). Phase velocities from seismic noise using beamforming and cross-correlation in Costa Rica and Nicaragua. *Geophysical Research Letters*, *35*(19). https://doi.org/10.1029/2008gl035387

Harmon, N., Rychert, C., & Gerstoft, P. (2010). Distribution of noise sources for seismic interferometry. *Geophysical Journal International*, *183*(3), 1470–1484. https://doi.org/10.1111/j.1365-246x.2010.04802.x

Hayes, J. L., Holbrook, W. S., Lizarralde, D., Van Avendonk, H. J., Bullock, A. D., Mora, M., et al. (2013). Crustal structure across the Costa Rican volcanic arc. *Geochemistry, Geophysics, Geosystems*, *14*(4), 1087–1103. https://doi.org/10.1002/ggge.20079

Hoernle, K., Abt, D. L., Fischer, K. M., Nichols, H., Hauff, F., Abers, G. A., et al. (2008). Arc-parallel flow in the mantle wedge beneath Costa Rica and Nicaragua. *Nature*, *451*(7182), 1094–1097. https://doi.org/10.1038/nature06550

Husen, S., Quintero, R., Kissling, E., & Hacker, B. (2003). Subduction-zone structure and magmatic processes beneath Costa Rica constrained by local earthquake tomography and petrological modeling. *Geophysical Journal International*, *155*(1), 11–32. https://doi.org/10.1046/j.1365-246x.2003.01984.x

Jeddi, Z., Gudmundsson, O., & Tryggvason, A. (2017). Ambient-noise tomography of Katla volcano, south Iceland. *Journal of Volcanology and Geothermal Research*, *347*, 264–277. https://doi.org/10.1016/j.jvolgeores.2017.09.019

Kay, S. M., & Ramos, V. A. (Eds.) (2006). *Evolution of an Andean Margin: A Tectonic and Magmatic View from the Andes to the Neuquén Basin (35°–39°S Lat)* (Vol. *407*). Geological Society of America.

Keilis-Borok, V. I., Levshin, A., Yanovskaya, T., Lander, A., Bukchin, B., Barmin, M., et al. (1989). *Seismic surface waves in a laterally inhomogeneous Earth* (Vol. 149). Springer.

Kellogg, J. N., Vega, V., Stallings, T., & Aiken, C. L. (1995). *Tectonic development of Panama, Costa Rica, and the Colombian Andes: Constraints from global positioning system geodetic studies and gravity* (p. 75). Special Papers-Geological Society of America. https://doi.org/10.1130/spe295-p75

Kobayashi, D., LaFemina, P., Geirsson, H., Chichaco, E., Abrego, A. A., Mora, H., & Camacho, E. (2014). Kinematics of the western Caribbean: Collision of the Cocos ridge and upper plate deformation. *Geochemistry, Geophysics, Geosystems*, *15*(5), 1671–1683. https://doi.org/10.1002/2014gc005234

Koulakov, I., Jaxybulatov, K., Shapiro, N. M., Abkadyrov, I., Deev, E., Jakovlev, A., et al. (2014). Asymmetric caldera-related structures in the area of the Avacha group of volcanoes in Kamchatka as revealed by ambient noise tomography and deep seismic sounding. *Journal of Volcanology and Geothermal Research*, *285*, 36–46. https://doi.org/10.1016/j.jvolgeores.2014.08.012

LaFemina, P., Dixon, T. H., Govers, R., Norabuena, E., Turner, H., Saballos, A., et al. (2009). Fore-arc motion and Cocos ridge collision in Central America. *Geochemistry, Geophysics, Geosystems*, *10*(5). https://doi.org/10.1029/2008gc002181

Landisman, M., Dziewonski, A., & Sato, Y. (1969). Recent improvements in the analysis of surface wave observations. *Geophysical Journal International*, *17*(4), 369–403. https://doi.org/10.1111/j.1365-246x.1969.tb00246.x

Lehujeur, M., Vergne, J., Maggi, A., & Schmittbuhl, J. (2016). Ambient noise tomography with non-uniform noise sources and low aperture networks: Case study of deep geothermal reservoirs in northern Alsace, France. *Geophysical Supplements to the Monthly Notices of the Royal Astronomical Society*, *208*(1), 193–210. https://doi.org/10.1093/gji/ggw373

Lin, F.-C., Li, D., Clayton, R. W., & Hollis, D. (2013). High-resolution 3D shallow crustal structure in Long Beach, California: Application of ambient noise tomography on a dense seismic array. *Geophysics*, *78*(4), Q45–Q56. https://doi.org/10.1190/geo2012-0453.1

Liu, X., Ben-Zion, Y., & Zigone, D. (2016). Frequency domain analysis of errors in cross-correlations of ambient seismic noise. *Geophysical Supplements to the Monthly Notices of the Royal Astronomical Society*, *207*(3), 1630–1652. https://doi.org/10.1093/gji/ggw361

Lobkis, O. I., & Weaver, R. L. (2001). On the emergence of the Green's function in the correlations of a diffuse field. *Journal of the Acoustical Society of America*, *110*(6), 3011–3017. https://doi.org/10.1121/1.1417528

Lücke, O. H., Götze, H.-J., & Alvarado, G. E. (2010). A constrained 3D density model of the upper crust from gravity data interpretation for Central Costa Rica. *International Journal of Geophysics*. https://doi.org/10.1155/2010/860902

Lundgren, P., & Russo, R. (1996). Finite element modeling of crustal deformation in the North America-Caribbean plate boundary zone. *Journal of Geophysical Research: Solid Earth*, *101*(B5), 11317–11327. https://doi.org/10.1029/95jb03747

Luo, Y., Yang, Y., Xu, Y., Xu, H., Zhao, K., & Wang, K. (2015). On the limitations of interstation distances in ambient noise tomography. *Geophysical Journal International*, *201*(2), 652–661. https://doi.org/10.1093/gji/ggv043

Lupi, M., Fuchs, F., & Pacheco, J. F. (2014). Fault reactivation due to the M7.6 Nicoya earthquake at the Turrialba-Irazú volcanic complex, Costa Rica: Effects of dynamic stress triggering. *Geophysical Research Letters*, *41*(12), 4142–4148. https://doi.org/10.1002/2014gl059942

MacMillan, I., Gans, P. B., & Alvarado, G. E. (2004). Middle Miocene to present plate tectonic history of the southern Central American Volcanic Arc. *Tectonophysics*, *392*(1–4), 325–348. https://doi.org/10.1016/j.tecto.2004.04.014

Macquet, M., Paul, A., Pedersen, H. A., Villaseñor, A., Chevrot, S., Sylvander, M., et al. (2014). Ambient noise tomography of the Pyrenees and the surrounding regions: Inversion for a 3D V_s model in the presence of a very heterogeneous crust. *Geophysical Journal International*, *199*(1), 402–415. https://doi.org/10.1093/gji/ggu270

Marshall, J. S., Fisher, D. M., & Gardner, T. W. (2000). Central Costa Rica deformed belt: Kinematics of diffuse faulting across the western Panama block. *Tectonics*, *19*(3), 468–492. https://doi.org/10.1029/1999tc001136

Martini, F., Tassi, F., Vaselli, O., Del Potro, R., Martinez, M., Van del Laat, R., & Fernandez, E. (2010). Geophysical, geochemical and geodetical signals of reawakening at Turrialba volcano (Costa Rica) after almost 150 yr of quiescence. *Journal of Volcanology and Geothermal Research*, *198*(3–4), 416–432. https://doi.org/10.1016/j.jvolgeores.2010.09.021

Melnick, D., & Echtler, H. P. (2006). Morphotectonic and geologic digital map compilations of the south-central Andes (36°–42°S). In *The Andes* (pp. 565–568). Springer.

Mickus, K. (2003). Gravity constraints on the crustal structure of Central America. In *AAPG Special Volumes*. https://doi.org/10.1306/m79877c29

Molnar, P., & Sykes, L. R. (1969). Tectonics of the Caribbean and Middle America regions from focal mechanisms and seismicity. *The Geological Society of America Bulletin*, *80*(9), 1639–1684. https://doi.org/10.1130/0016-7606(1969)80[1639:totcam]2.0.co;2

Montero, W. (2001). *Neotectónica de la región central de Costa Rica: Frontera oeste de la microplaca de Panamá*. Revista Geológica de América Central.

Montero, W., Rojas, W., & Linkimer, L. (2013). *Neotectónica de las fallas Ochomogo y Capellades y su relación con el sistema de falla Aguacaliente, falda sur macizo Irazú-Turrialba, Costa Rica* (Vol. 48, pp. 119–139). Revista Geológica de América Central.

Montero-Pohly, W. (2021a). *Análisis retrospectivo del terremoto de Limón del 22 de abril de 1991 (Mw 7, 7) y de la actividad sísmica disparada en las fallas Ayil, Pacuare, Atirro, División y Navarro* (Vol. 65, pp. 1–26). Revista Geológica de América Central.

Montero-Pohly, W. (2021b). *Los terremotos de Cuericí del 24 de abril de 1991 (Mw 6, 1) y de Buenavista del 3 de julio de 1983 (Ms 6, 3): Dos rupturas contiguas de la falla división en el centro de Costa Rica* (Vol. 65. pp. 1–22). Revista Geológica de América Central.

Mordret, A., Landès, M., Shapiro, N., Singh, S., & Roux, P. (2014). Ambient noise surface wave tomography to determine the shallow shear velocity structure at Valhall: Depth inversion with a neighbourhood algorithm. *Geophysical Journal International*, *198*(3), 1514–1525. https://doi.org/10.1093/gji/ggu217

Mordret, A., Landès, M., Shapiro, N., Singh, S., Roux, P., & Barkved, O. (2013). Near-surface study at the Valhall oil field from ambient noise surface wave tomography. *Geophysical Journal International*, *193*(3), 1627–1643. https://doi.org/10.1093/gji/ggt061

Mordret, A., Rivet, D., Landès, M., & Shapiro, N. M. (2015). Three-dimensional shear velocity anisotropic model of Piton de la Fournaise volcano (La Réunion Island) from ambient seismic noise. *Journal of Geophysical Research: Solid Earth*, *120*(1), 406–427. https://doi.org/10.1002/2014jb011654

Nazarian, S., Stokoe, K. H., II, & Hudson, W. R. (1983). Use of spectral analysis of surface waves method for determination of moduli and thicknesses of pavement systems (Vol. *930*).

Nicolson, H., Curtis, A., Baptie, B., & Galetti, E. (2012). Seismic interferometry and ambient noise tomography in the British Isles. *Proceedings of the Geologists' Association*, *123*(1), 74–86. https://doi.org/10.1016/j.pgeola.2011.04.002

Nishida, K., Kawakatsu, H., & Obara, K. (2008). Three-dimensional crustal *S* wave velocity structure in Japan using microseismic data recorded by Hi-net tiltmeters. *Journal of Geophysical Research: Solid Earth*, *113*(B10). https://doi.org/10.1029/2007jb005395

Norabuena, E., Dixon, T. H., Schwartz, S., DeShon, H., Newman, A., Protti, M., et al. (2004). Geodetic and seismic constraints on some seismogenic zone processes in Costa Rica. *Journal of Geophysical Research: Solid Earth*, *109*(B11). https://doi.org/10.1029/2003jb002931

Nuñez, E., Schimmel, M., Stich, D., & Iglesias, A. (2020). Crustal velocity anomalies in Costa Rica from ambient noise tomography. *Pure and Applied Geophysics*, *177*(2), 941–960. https://doi.org/10.1007/s00024-019-02315-z

Obermann, A., Planes, T., Hadziioannou, C., & Campillo, M. (2016). Lapse-time-dependent coda-wave depth sensitivity to local velocity perturbations in 3D heterogeneous elastic media. *Geophysical Journal International*, *207*(1), 59–66. https://doi.org/10.1093/gji/ggw264

Obermann, A., Planes, T., Larose, E., & Campillo, M. (2013). Imaging preeruptive and coeruptive structural and mechanical changes of a volcano with ambient seismic noise. *Journal of Geophysical Research: Solid Earth*, *118*(12), 6285–6294. https://doi.org/10.1002/2013jb010399

Park, C., Miller, R., & Xia, J. (1998). Imaging dispersion curves of surface waves on multi-channel record. Technical program with biographies. In *Society of exploration geophysics, 68th Annual Meeting, New Orleans, Louisiana*.

Planès, T., Obermann, A., Antunes, V., & Lupi, M. (2020). Ambient-noise tomography of the Greater Geneva Basin in a geothermal exploration context. *Geophysical Journal International*, *220*(1), 370–383. https://doi.org/10.1093/gji/ggz457

Ponce, D., & Case, J. (1987). Geophysical interpretation of Costa Rica. In *Mineral resources assesment of the Republic of Costa Rica* (pp. 1–1865). US Geological Survey Miscellaneous Iinvestigations.

Power, J. A., Roman, D. C., Nicolaysen, K. P., Izbekov, P. E., Werner, C. A., Janiszewski, H. A., et al. (2020). Multi-disciplinary evidence for a large, previously unrecognized caldera in the islands of four mountains, Central Aleutian Arc, Alaska. In *AGU Fall Meeting 2020*.

Pritchard, M. E., & Gregg, P. M. (2016). Geophysical evidence for silicic crustal melt in the continents: Where, what kind, and how much? *Elements*, *12*(2), 121–127. https://doi.org/10.2113/gselements.12.2.121

Protti, M., Schwartz, S. Y., & Zandt, G. (1996). Simultaneous inversion for earthquake location and velocity structure beneath Central Costa Rica. *Bulletin of the Seismological Society of America*, *86*(1A), 19–31. https://doi.org/10.1785/bssa08601a0019

Ritzwoller, M. H., Lin, F.-C., & Shen, W. (2011). Ambient noise tomography with a large seismic array. *Comptes Rendus Geoscience*, *343*(8–9), 558–570. https://doi.org/10.1016/j.crte.2011.03.007

Rix, G. J. (1990). Experimental study of factors affecting the spectral-analysis-of-surface-waves method. In *Transportation Research Information Services (TRIS) and International Transport Research Documentation (ITRD) databases*.

Rizzo, A. L., Di Piazza, A., de Moor, J. M., Alvarado, G. E., Avard, G., Carapezza, M. L., & Mora, M. M. (2016). Eruptive activity at Turrialba volcano (Costa Rica): Inferences from $^{3}He/^{4}He$ in fumarole gases and chemistry of the products ejected during 2014 and 2015. *Geochemistry, Geophysics, Geosystems*, *17*(11), 4478–4494. https://doi.org/10.1002/2016gc006525

RSN. (2011). *Network information*. FDSN Network Information, Universidad de Costa Rica, TC: Red Simológica Nacional (RSN). https://doi.org/10.15517/TC

Rychert, C. A., Fischer, K. M., Abers, G. A., Plank, T., Syracuse, E., Protti, J., et al. (2008). Strong along-arc variations in attenuation in the mantle wedge beneath Costa Rica and Nicaragua. *Geochemistry, Geophysics, Geosystems*, *9*(10). https://doi.org/10.1029/2008gc002040

Sadofsky, S. J., Portnyagin, M., Hoernle, K., & van den Bogaard, P. (2008). Subduction cycling of volatiles and trace elements through the Central American Volcanic Arc: Evidence from melt inclusions. *Contributions to Mineralogy and Petrology*, *155*(4), 433–456. https://doi.org/10.1007/s00410-007-0251-3

Sak, P. B., Fisher, D. M., Gardner, T. W., Marshall, J. S., & LaFemina, P. C. (2009). Rough crust subduction, forearc kinematics, and Quaternary uplift rates, Costa Rican segment of the Middle American Trench. *The Geological Society of America Bulletin*, *121*(7–8), 992–1012. https://doi.org/10.1130/b26237.1

Sallarès, V., Dañobeitia, J. J., & Flueh, E. (2000). Seismic tomography with local earthquakes in Costa Rica. *Tectonophysics*, *329*(1–4), 61–78. https://doi.org/10.1016/s0040-1951(00)00188-8

Sambridge, M. (1999). Geophysical inversion with a neighborhood algorithm—I. Searching a parameter space. *Geophysical Journal International*, *138*(2), 479–494. https://doi.org/10.1046/j.1365-246x.1999.00876.x

Shapiro, N., Campillo, M., Stehly, L., & Ritzwoller, M. H. (2005). High-resolution surface-wave tomography from ambient seismic noise. *Science*, *307*(5715), 1615–1618. https://doi.org/10.1126/science.1108339

Shapiro, N., & Ritzwoller, M. (2002). Monte-Carlo inversion for a global shear-velocity model of the crust and upper mantle. *Geophysical Journal International*, *151*(1), 88–105. https://doi.org/10.1046/j.1365-246x.2002.01742.x

Sheen, D.-H., & Shin, J. S. (2016). Observation of continuous microseismic *P* waves in Asia. *Journal of Geophysical Research: Solid Earth*, *121*(1), 248–259. https://doi.org/10.1002/2015jb012420

Shen, J., Molisch, A. F., & Salmi, J. (2012). Accurate passive location estimation using TOA measurements. *IEEE Transactions on Wireless Communications*, *11*(6), 2182–2192. https://doi.org/10.1109/twc.2012.112012.120104

Sigmundsson, F. (2016). New insights into magma plumbing along rift systems from detailed observations of eruptive behavior at Axial volcano. *Geophysical Research Letters*, *43*(24), 12–423. https://doi.org/10.1002/2016gl071884

Singer, J., Obermann, A., Kissling, E., Fang, H., Hetényi, G., & Grujic, D. (2017). Along-strike variations in the Himalayan orogenic wedge structure in Bhutan from ambient seismic noise tomography. *Geochemistry, Geophysics, Geosystems*, *18*(4), 1483–1498. https://doi.org/10.1002/2016gc006742

Stankiewicz, J., Ryberg, T., Haberland, C., Fauzi, & Natawidjaja, D. (2010). Lake Toba volcano magma chamber imaged by ambient seismic noise tomography. *Geophysical Research Letters*, *37*(17). https://doi.org/10.1029/2010gl044211

Stehly, L., Campillo, M., & Shapiro, N. (2006). A study of the seismic noise from its long-range correlation properties. *Journal of Geophysical Research: Solid Earth*, *111*(B10). https://doi.org/10.1029/2005jb004237

Stoiber, R., & Carr, M. (1973). Quaternary volcanic and tectonic segmentation of Central America. *Bulletin Volcanologique*, *37*(3), 304–325. https://doi.org/10.1007/bf02597631

Syracuse, E. M., Abers, G. A., Fischer, K., MacKenzie, L., Rychert, C., Protti, M., et al. (2008). Seismic tomography and earthquake locations in the Nicaraguan and Costa Rican upper mantle. *Geochemistry, Geophysics, Geosystems*, *9*(7). https://doi.org/10.1029/2008gc001963

Takei, Y. (2002). Effect of pore geometry on V_p/V_s: From equilibrium geometry to crack. *Journal of Geophysical Research: Solid Earth*, *107*(B2), ECV6-1–ECV6-12. https://doi.org/10.1029/2001jb000522

Tarantola, A. (2005). *Inverse problem theory and methods for model parameter estimation*. SIAM.

Tarantola, A., & Valette, B. (1982). Generalized nonlinear inverse problems solved using the least squares criterion. *Reviews of Geophysics*, *20*(2), 219–232. https://doi.org/10.1029/rg020i002p00219

Thorpe, R., Locke, C., Brown, G., Francis, P., & Randal, M. (1981). Magma chamber below Poás volcano, Costa Rica. *Journal of the Geological Society*, *138*(3), 367–373. https://doi.org/10.1144/gsjgs.138.3.0367

Trenkamp, R., Kellogg, J. N., Freymueller, J. T., & Mora, H. P. (2002). Wide plate margin deformation, southern Central America and northwestern South America, CASA GPS observations. *Journal of South American Earth Sciences*, *15*(2), 157–171. https://doi.org/10.1016/s0895-9811(02)00018-4

Vannucchi, P., & Morgan, J. P. (2019). Overview of the tectonics and geodynamics of Costa Rica. In *Poás volcano* (pp. 1–12). Springer. https://doi.org/10.1007/978-3-319-02156-0_1

Vargas, C. A., & Mann, P. (2013). Tearing and breaking off of subducted slabs as the result of collision of the Panama Arc-Indenter with northwestern South America. *Bulletin of the Seismological Society of America*, *103*(3), 2025–2046. https://doi.org/10.1785/0120120328

Vaselli, O., Tassi, F., Duarte, E., Fernandez, E., Poreda, R., & Huertas, A. D. (2010). Evolution of fluid geochemistry at the Turrialba volcano (Costa Rica) from 1998 to 2008. *Bulletin of Volcanology*, *72*(4), 397–410. https://doi.org/10.1007/s00445-009-0332-4

Villegas Alvarez, R. J., Petrinovic, I. A., & Carniel, R. (2019). *S* wave velocity zones at the Irazú Volcano (Costa Rica). *Journal of South American Earth Sciences*.

Wathelet, M. (2005). *Array recordings of ambient vibrations: Surface-wave inversion (Ph.D. dissertation)* (p. 161). Liége University.

Wathelet, M. (2008). An improved neighborhood algorithm: Parameter conditions and dynamic scaling. *Geophysical Research Letters*, *35*(9). https://doi.org/10.1029/2008gl033256

Wespestad, C. E., Thurber, C. H., Andersen, N. L., Singer, B. S., Cardona, C., Zeng, X., et al. (2019). Magma reservoir below Laguna del Maule volcanic field, Chile, imaged with surface-wave tomography. *Journal of Geophysical Research: Solid Earth*, *124*(3), 2858–2872. https://doi.org/10.1029/2018jb016485

Yang, Y., Ritzwoller, M. H., Lin, F.-C., Moschetti, M., & Shapiro, N. M. (2008). Structure of the crust and uppermost mantle beneath the western United States revealed by ambient noise and earthquake tomography. *Journal of Geophysical Research: Solid Earth*, *113*(B12). https://doi.org/10.1029/2008jb005833

Yao, H., Beghein, C., & Van Der Hilst, R. D. (2008). Surface wave array tomography in SE Tibet from ambient seismic noise and two-station analysis-II. Crustal and upper-mantle structure. *Geophysical Journal International*, *173*(1), 205–219. https://doi.org/10.1111/j.1365-246x.2007.03696.x

Yao, H., & Van Der Hilst, R. D. (2009). Analysis of ambient noise energy distribution and phase velocity bias in ambient noise tomography, with application to SE Tibet. *Geophysical Journal International*, *179*(2), 1113–1132. https://doi.org/10.1111/j.1365-246x.2009.04329.x

Yao, Z., Quintero, R., & Roberts, R. (1999). Tomographic imaging of *P* and *S* wave velocity structure beneath Costa Rica. *Journal of Seismology*, *3*(2), 177–190. https://doi.org/10.1023/a:1009885321799

Zhang, J., Gerstoft, P., & Bromirski, P. D. (2010). Pelagic and coastal sources of *P* wave microseisms: Generation under tropical cyclones. *Geophysical Research Letters*, *37*(15). https://doi.org/10.1029/2010gl044288

Zhang, S. X., & Chan, L. S. (2003). Possible effects of misidentified mode number on Rayleigh wave inversion. *Journal of Applied Geophysics*, *53*(1), 17–29. https://doi.org/10.1016/s0926-9851(03)00014-4

Zigone, D., Ben-Zion, Y., Campillo, M., & Roux, P. (2015). Seismic tomography of the Southern California plate boundary region from noise-based Rayleigh and Love waves. *Pure and Applied Geophysics*, *172*(5), 1007–1032. https://doi.org/10.1007/s00024-014-0872-1